BRNO UNIVERSITY OF TECHNOLOGY

VYSOKÉ UČENÍ TECHNICKÉ V BRNĚ

FACULTY OF MECHANICAL ENGINEERING

FAKULTA STROJNÍHO INŽENÝRSTVÍ

INSTITUTE OF MANUFACTURING TECHNOLOGY

ÚSTAV STROJÍRENSKÉ TECHNOLOGIE

ADVANCED TECHNOLOGY FOR 3D PRINTING OF METAL PARTS AND THEIR MACHINING

POKROČILÉ TECHNOLOGIE 3D TISKU KOVOVÝCH DÍLŮ A JEJICH OBRÁBĚNÍ

SHORT VERSION OF PH.D. THESIS
ZKRÁCENÁ VERZE PH.D. THESIS

AUTHOR
AUTOR PRÁCE

Ing. Martin Malý

SUPERVISOR
VEDOUCÍ PRÁCE

doc. Ing. Jan Zouhar, Ph.D.

SUPERVISOR SPECIALIST

VEDOUCÍ PRÁCE – SPECIALISTA

prof. Ing. Pavel Václavek, Ph.D.

BRNO 2025

ABSTRACT

The present dissertation investigates the advanced technology of 3D printing of metal parts using material extrusion (MEX) with H13 tool steel, and evaluates the influence of post-processing and machining on the final part performance. The primary objective of this study was to establish a correlation between printing parameters, porosity, microstructure, mechanical properties, and machinability. As-built samples exhibited an average porosity of 4.76 %, which significantly limited tensile strength (UTS ~1200 MPa) and ductility (<1 %). Conventional heat treatment reduced porosity to 1.87 %, whereas hot isostatic pressing (HIP) combined with heat treatment decreased it to 0.48 %, yielding a substantial improvement in mechanical properties. The HIP + HT samples demonstrated a yield strength of approximately 1300 MPa, an ultimate tensile strength of around 1550 MPa and ductility 8 %. In terms of machinability, it has been proven that increasing the feed rate per tooth leads to an increase in cutting forces during machining, which results in increased tool wear and increased surface roughness of the material.

Keywords

H13 tool steel, material extrusion, additive manufacturing, mechanical properties

CONTENT

1 INTRODUCTION

The beginning of the 21st century has been marked by the rapid and dynamic evolution of additive manufacturing (AM), a technology that is progressively becoming a central pillar in advanced manufacturing systems. Additive manufacturing encompasses a suite of techniques for fabricating objects directly from digital models by depositing material layer by layer, representing a paradigmatic shift from traditional methods such as machining or casting. This transition is not only technological but also conceptual, offering new possibilities in terms of how products are designed, customized, and produced. The central advantage of AM lies in its ability to fabricate complex geometries and integrated features without the need for specialized tooling or extensive manual intervention.

Initially characterized as a tool for rapid prototyping, additive manufacturing has matured into a robust production technology. This evolution has been supported by international standardization efforts, most notably the ASTM F2792-12 and ISO/ASTM 52900:2021 frameworks, which formally define AM as a process of building objects layer by layer from 3D digital data [1; 2]. These standards also offer a taxonomy for categorizing the various AM technologies and materials, thereby facilitating clearer communication, quality control, and regulatory compliance across disciplines and industries. The shift in nomenclature from “rapid prototyping” to “additive manufacturing” reflects not only technological advances but also a broader conceptual understanding of AM as a viable alternative for end-use part production.

From a process perspective, additive manufacturing methods are often classified into two main categories based on their operational mechanics: two-phase and single-phase processes. Two-phase processes involve distinct shaping and consolidation stages. Techniques such as binder jetting and material extrusion exemplify this approach. In these processes, a precursor or “green” part is first formed using binders or thermoplastic matrices. This intermediate structure is then subjected to thermal post-processing steps, such as debinding and sintering, to achieve the desired mechanical and microstructural properties. The final material characteristics are thus significantly influenced by the parameters of both the shaping and consolidation phases, including temperature gradients, atmosphere control, and shrinkage behaviour.

In contrast, single-phase processes integrate shaping and consolidation into a single step. These include powder bed fusion (PBF) methods such as laser beam melting (LBM), direct metal laser sintering (DMLS), selective laser melting (SLM), and electron beam melting (EBM). These techniques utilize high-energy beams to selectively melt and fuse metal powders in a layer-wise fashion. The advantages of single-phase processes include high resolution, excellent mechanical properties, and reduced post-processing requirements. However, they also present challenges such as residual stress formation, anisotropy, and surface roughness. The selection of appropriate scan strategies, support structures, and process parameters is therefore critical to achieving consistent part quality.

The application landscape of additive manufacturing has expanded significantly across multiple industrial domains. In the aerospace sector, AM facilitates lightweighting, part consolidation, and the production of complex, performance-optimized structures. In medicine, it enables patient-specific implants, surgical tools, and biocompatible scaffolds for tissue engineering. In the automotive industry, AM supports tooling, customization, and small-series production. The tool and die sector, in particular, has shown increasing interest in AM due to its potential to reduce lead times and improve cooling performance through conformal channel integration.

Despite the diversity of additive manufacturing methods, they all share a common digital foundation. The AM workflow begins with the creation of a 3D model in computer-aided design (CAD) software, followed by its conversion into a series of layers via slicing algorithms. This layer by layer information is then translated into machine instructions that guide the deposition

or fusion of material. The digital nature of AM not only enables design flexibility but also facilitates integration with advanced simulation tools, real-time process monitoring, and quality assurance systems. These capabilities are essential for transitioning AM from prototyping to reliable, repeatable production.

This dissertation aims to contribute to this evolving field by investigating the use of material extrusion techniques for processing tool steels, with a particular focus on understanding the relationship between process parameters, material behaviour, and final part performance. The research is motivated by the need for cost-effective, high-performance tooling solutions in industrial settings and seeks to address the technical challenges associated with feedstock development, thermal processing, and geometric fidelity. By bridging fundamental research with practical application, the work aspires to expand the industrial relevance of additive manufacturing and support its continued integration into advanced manufacturing ecosystems.

2 AIMS OF THE THESIS

Assignment: This scientific research work will focus on applications that are almost impossible to produce economically using standard technologies, advanced machining and finishing of functional surfaces for selected applications, and their safe use.

The original intention of the dissertation entitled “Advanced technologies for 3D printing of metal parts and their machining” was to analyse methods of 3D printing of metal parts, select a specific method and apply the selected technology in industry. After initial analysis and selection of material extrusion technology with regard to available resources, it was found that this method is not currently ready for its intended use in its current state. For this reason, various analyses were used to examine the material properties of the printed metal with the aim of improving its mechanical properties after printing.

Material extrusion is an economical and relatively simple additive manufacturing method. However, its application is limited by lower part density and mechanical properties when compared to powder-based technologies such as SLS or EBM. Recent studies have indicated the necessity of enhancing the reliability of the manufacturing process and optimising its parameters to improve the quality of the final printed components. This knowledge gap indicates that further studies are required to fully exploit material extrusion for broader industrial applications.

The defined objectives are:

- initial analysis of the current state of knowledge, recent trends, and 3D printing methods,
- selection of AM technology using metal materials and identify a suitable material for industrial application,
- analysis of the selected material and determine its key properties for the planned application,
- suggestion of post-processing to enhance material properties for the planned application,
- comparison of properties of selected AM method with conventional manufacturing technique,
- analysis of the “improved” material with regard to the planned application.

In terms of the above-defined objectives and research into the current state of knowledge in this area, it can be stated that no such study has been conducted to date and that it would be beneficial to both the scientific and professional communities.

3 MATERIALS AND METHODS

The experimental part was carried out in accordance with the objectives of this thesis. This part includes the selection of production technology, the design of testing methodology, the production and testing of samples. The main objective is to propose a procedure for improving the mechanical properties of samples.

3.1 AM technology and material selection

Material extrusion technology was chosen based on the available options and literature research. This technology is not as widely referenced in professional circles as other AM technologies. Unlike traditional metal AM systems, which require lasers or hazardous powders, the Studio System uses BMD – a process similar to FDM, whereby metal rods bound in polymer are extruded layer by layer. After printing, the parts are debound and sintered in a furnace to achieve full density.

The initial concept already considered the application of technology for the production of plastic injection molds with integrated cooling channels. Although this idea remains promising, it was not set as the main objective of the work. This is also reflected in the chosen material – H13 tool steel, which is suitable for this application due to its properties.

AISI H13 (W. Nr. 1.2344, DIN EN X40CrMoV5-1, ČSN 19 554) is a hardenable C-Cr-Mo-Si-V steel that is widely used around the world. It is used to produce moulds for plastic injection moulding. Here, high temperatures and a long fatigue life are expected [3-5]. The chemical composition of H13 steel is shown in Tab. 1. Shayfull et al. [6] state in their study that using internal cooling channels reduces injection moulding cycle times by up to 25 %, thereby increasing productivity. The complex geometry of internal cooling channels in moulds makes them a suitable candidate for additive manufacturing, as these channels would be almost impossible to produce by other manufacturing methods. Conventional manufacturing is limited to straight geometries when producing channels [4]. Production usually involves several separate parts that are joined together, typically by welding. These welds can affect the thermal properties of the material used in the mould, which can reduce its service life. When using additive technologies, however, the design of internal cooling channels is almost unlimited. Many studies have been conducted on additively manufactured H13 tool steel using either the Direct Energy Deposition (DED) method (see references [7-9] and others) or the Laser Powder Bed Fusion (LPBF) method (see references [10; 11] and others). However, as far as material extrusion and H13 steel are concerned, research in this area is not yet widespread and knowledge is limited. Therefore, there is room for further research.

Tab. 1 Chemical composition of H13 tool steel

Element	**C**	**Mn**	**Si**	**Cr**	**Ni**
(Weight. %)	0.32–0.45	0.20–0.50	0.80–1.20	4.75–5.50	0.30
Mo	**V**	**Cu**	**P**	**S**	**Fe**
1.10–1.75	0.80–1.20	0.25	0.25 max	0.03 max	Rest

The use of material from the manufacturer is an essential step in the process of utilising the Studio System technology. In order to verify the material, a SEM analysis of the input material was performed. It has been demonstrated that the material exhibits a chemical correspondence to H13 tool steel, the composition of which is presented in Tab. 1. As illustrated in Fig. 1 a), the material's structure has been determined through SEM analysis. It is evident that the structure comprises particles of varying dimensions. The black spots represent the material

binder. The distribution of particles is illustrated in Fig. 1 b). The material's particle distribution makes it well-suited for sintering.

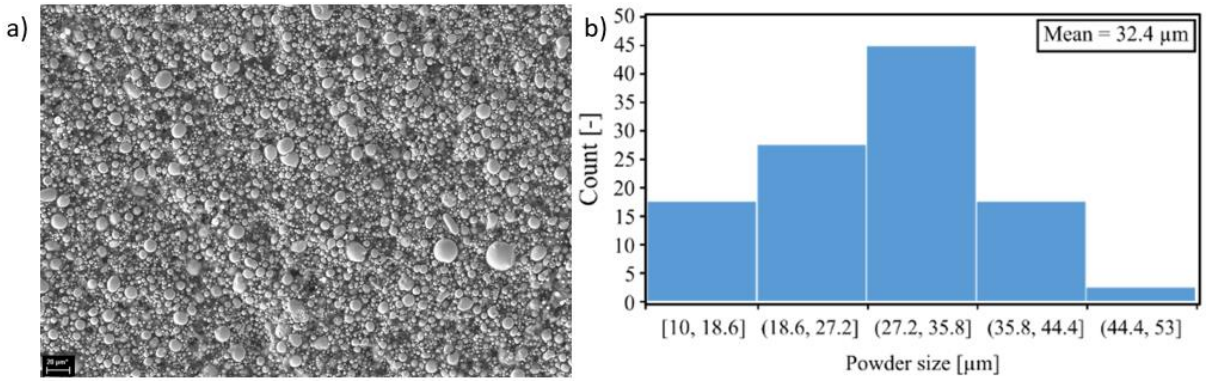

Fig. 1 Input rod SEM analysis structure, b) particle size distribution

3.2 Testing methodology

The testing methodology is based on the objectives defined for this work. Following an initial analysis of the input material, it became necessary to define the printed material. For this reason, a porosity analysis was performed, followed by tensile testing. This determined the basic mechanical properties, after which the material was machined, a process closely related to the proposed objectives. Subsequently, the focus shifted to improving post-processing, specifically heat treatment and HIP. Finally, the effect of the printing direction on the machining direction was investigated. A simplified workflow is shown in Fig. 2.

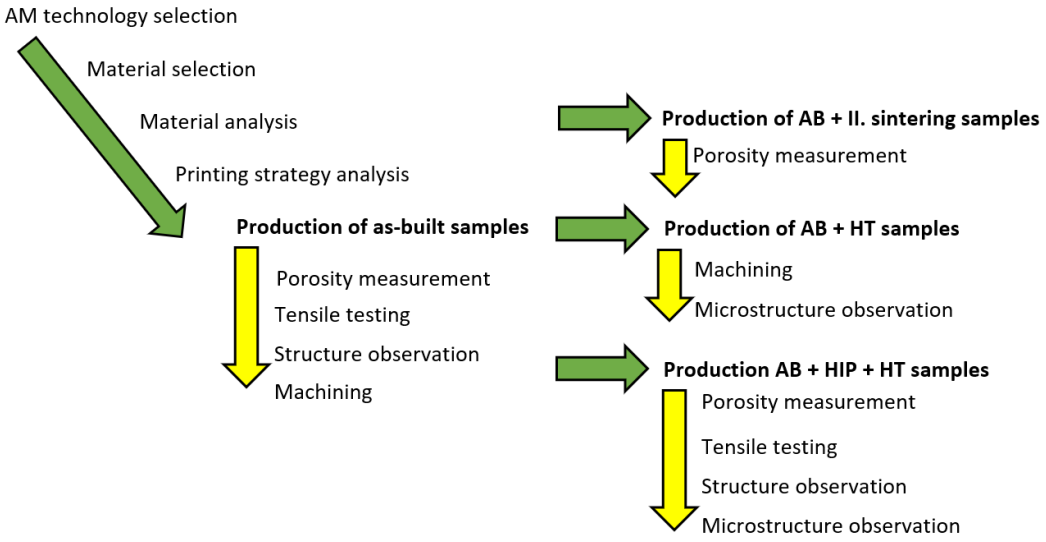

Fig. 2 Simplified workflow

Samples were created in five series.

- 1st series for tensile testing of as-built samples,
- 2nd series for machining of as-built samples,
- 3rd series for machining samples after heat treatment,
- 4th series for tensile testing after HIP and
- 5th series for analysis of influence of printing direction on the machining direction.

The basic printing parameters are listed in the Tab. 2. Since a closed-loop printing system was used, most parameters cannot be modified during the printing process.

Tab. 2 Printing parameters

Nozzle diameter (mm)	Layer height (mm)	Printing strategy (-)	Nozzle temperature (°C)	Bed temperature (°C)	Printing speed ($mm.s^{-1}$)	Chamber temperature (°C)
0,4	0,1	Alternating lines	175	65	15	50

3.3 Technologies and Measurement Instruments

This chapter is devoted to devices used for sample analysis.

In order to perform mechanical property tests, the type of tests first had to be formulated. A destructive tensile test was performed in accordance with ČSN EN ISO 6892-1 Metallic materials - Tensile testing - Part 1 [12], was selected for the experimental investigation. The samples were produced using 3D printing and subsequent machining. The dimensions of the sample for the tensile test were selected on the basis of economic factors, with the tested diameter set at 6 mm and the total length of the sample fixed at 60 mm.

The surface roughness of the printed samples was measured using a T4 contour graph. A diamond tip was used to measure individual surfaces and subsequently evaluate surface roughness. Closer surface observation was carried out with the Alicona Infinite Focus G5 (Bruker Corp., USA). The wear on the milling cutters after machining was recorded using a ZEISS Stemi 2000-C microscope. Tool wear during machining was measured using a KEYENCE VHX F microscope. Measuring the tool wear using KEYENCE microscope was used for higher resolution in comparison to ZEISS microscope. Scanning electron microscope Tescan Vega (Tescan Orsay Holding as. Czechia) was used for tool wear analysis after the tests. Rockwell hardness testing was performed using a Zwick/Roell ZHR hardness tester. measurement was done at LECO 247 INNOVATEST Prague Czech Republic. The cutting forces were monitored using a KISTLER 9272 dynamometer. Tensile testing was done according to CSN EN ISO 6892-1 on Zwick/Roell Z250 with loadcell 150 kN and extensometer MultiXtens. Samples for microstructure observation were prepared using LECO MSX metallographic cut-off saw and pressing it into a puck. Subsequently the samples were grounded and polished with diamond paste of 1 µm and 0.5 µm. After polishing the samples were etched using 2 % nital solution. Microstructure was observed at Olympus DSX500 microscope.

Porosity was measured by the optical microscope Olympus DSX 500 with plugin for porosity evaluation and evaluated by ImageJ software. Measurements were performer under 140 magnification. The overall porosity was subsequently checked using CT scan.

SEM analysis was done using scanning electron microscope (FEG-SEM, Ultra Plus, Carl Zeiss AG, Germany) equipped with electron backscatter diffraction (EBSD) detector (Nordlys Nano, Oxford Instruments, UK). EBSD analyses were performed on samples polished using standard metallographic methods, including final polishing with 0.7 µm diamond paste and subsequent vibro-polishing (QPol Vibro, QaTM GmbH, Germany) for 1.5 hours in 0.05 µm colloidal silica.

Heat treatment was done under inert atmosphere. Quenching and tempering was done according following steps: heating up 1035 °C (222 °C/h) for 35 min in argon protective atmosphere, cooled in the air, first tempering at 600 °C/4 h and the second at 575 °C/4 h and air cooled both at ambient temperature. HIPping was done under 1150 °C held time 2 hours and pressure 190 MPa.

4 RESULTS

This chapter presents a summary of the results carried out during this thesis. It contains major results from the published articles. It is divided into 4 main subsections according to used post-processing technology. They are:

- as-built samples,
- machining after HT,
- influence of the printing direction on the machinability,
- HIP + HT.

4.1 As-built samples

A comparative analysis was conducted on three categories of additively manufactured samples, which were then analysed in conjunction with reference materials produced conventionally by rolling. The sample designations are listed in Tab. 3.

Tab. 3 Description of samples tensile test of 1st sample series

Groups description of the samples	Label
Referenced as-rolled material	A
Horizontally as-built with the allowance for machining	B
Vertically as-built	C
Horizontally as-built without the allowance for machining	D

Samples marked C (printed vertically) were machined along their entire length, as were samples B (printed horizontally with allowance for machining). Conversely, samples D were subjected to machining exclusively at the thread locations. The hypothesis was that the hardened surface layer could affect the mechanical properties of the sample.

In addition to the samples intended for tensile testing, those designated for machinability testing were also prepared. The characterisation of these samples is outlined in the following chapter, entitled “AB Samples for machining”.

4.1.1 Tensile testing

Fig. 3 shows the results of tensile testing of several types of samples, as shown in Tab. 3. The tensile test evaluated the yield strength, tensile strength, and elongation of the printed samples together with the reference material. Compared to the reference material, the samples produced using additive technology achieved higher values for tensile strength and yield strength. The higher tensile strength values are likely due to the heat treatment (sintering) involved in the 3D printing process itself. The ductility of the printed samples was around 2 %. Novak et al. [13] studied 17-4 PH steel created using material extrusion and achieved a value of 4.5 ± 0.3 %. The yield strength ($R_{p0.2}$) was not measured at vertically printed samples. In the case of vertically printed samples, no elastic deformation was observed, and the lowest UTS was recorded. It is therefore inadvisable to employ this particular printing direction.

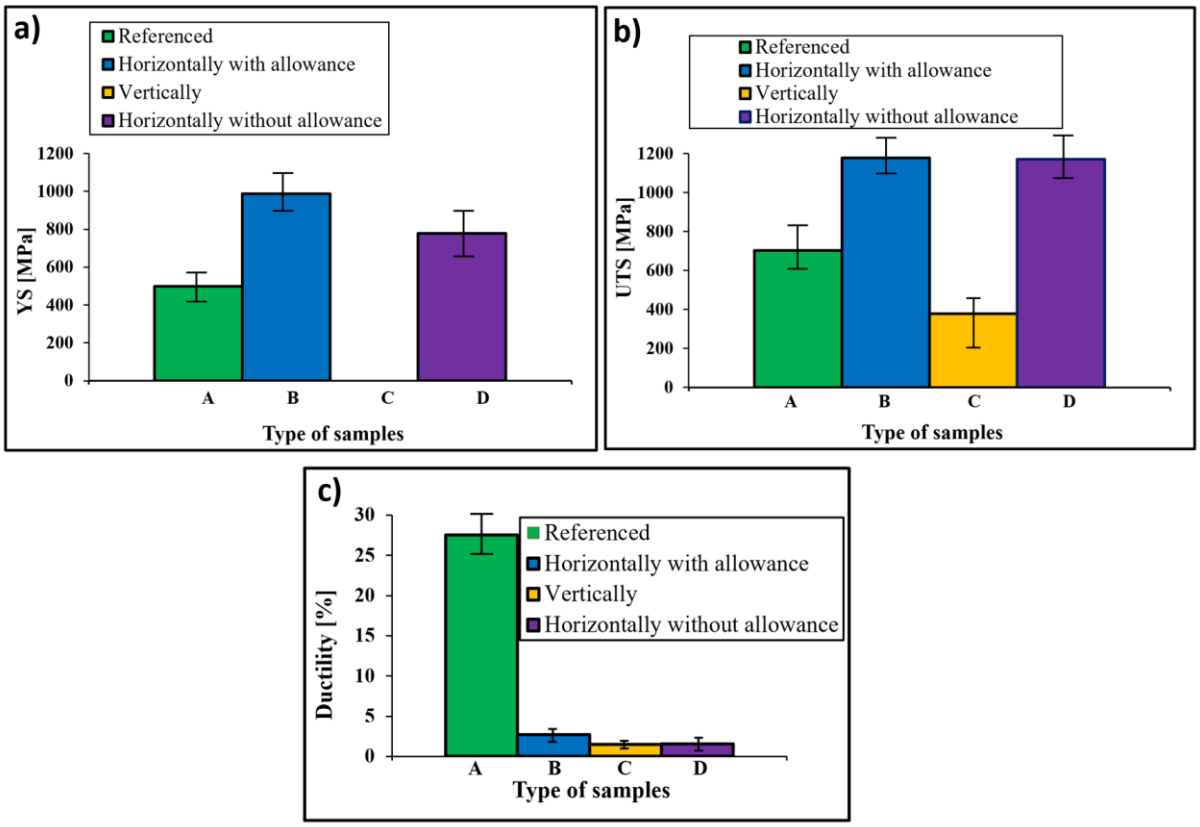

Fig. 3 Mechanical properties of samples
a) yield strength, b) ultimate tensile strength, c) ductility

The fracture surface of the vertically printed samples (C) exhibits a distinctive “stair-step” or “terrace-like” morphology, indicative of the build direction. The presence of pronounced striations and cracks in the deposition layers indicates inadequate interlayer bonding and results in brittle fracture. This is consistent with the low tensile strength and almost negligible ductility. The cross-section of samples printed in the horizontal direction after the tensile test is shown in Fig. 4 b) and d), where pores between the individual layers are visible. In this case, the separation of the layers began at the boundary of the holes (pores) between the individual layers. When the mechanical properties of the two types of samples printed in the horizontal direction were compared, no statistically significant difference was observed. The measured values demonstrate that machining exerts no effect on the resulting mechanical properties. The fracture surface of the reference sample (Fig. 4 a)) exhibits a ductile fracture morphology, characterised by the presence of noticeable dimples and radially distributed shear lips. This finding is indicative of substantial plastic deformation prior to failure, a conclusion that is further corroborated by the observation of high ductility (~27 %) during mechanical testing.

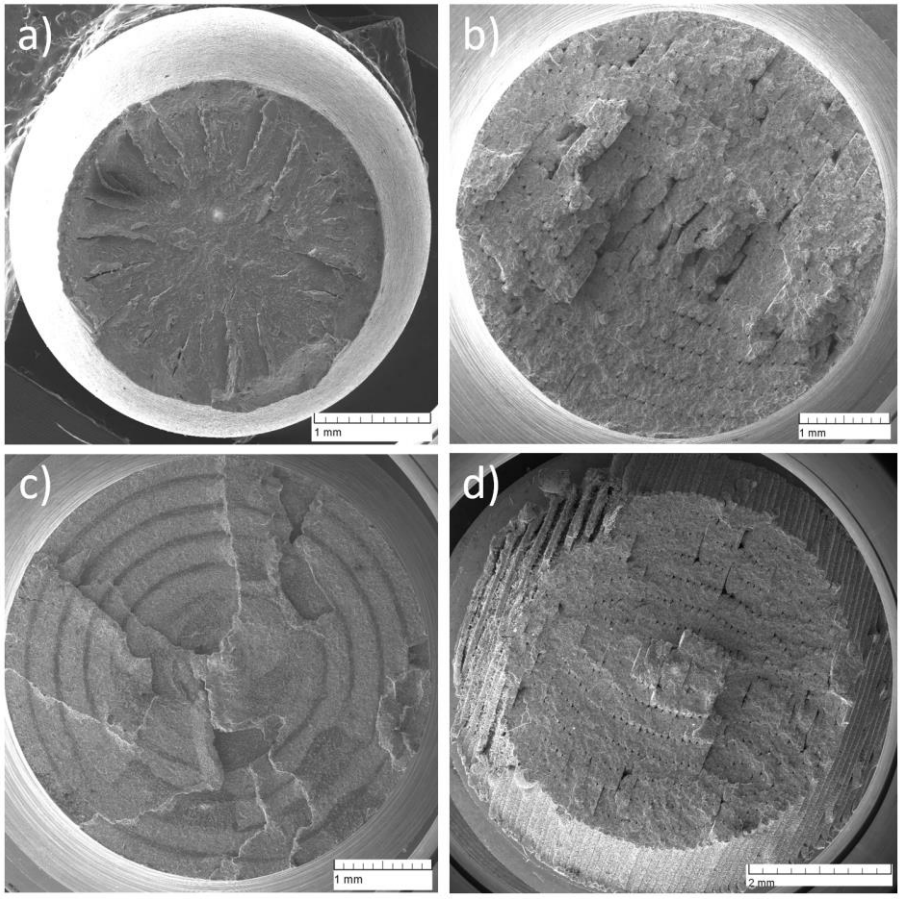

Fig. 4 SEM images of the fracture surfaces of each group of samples.
Referenced samples A, b) horizontally printed samples with allowance B, c) vertically printed samples C, d) horizontally printed samples without allowance D.

The SEM analysis corroborates the outcomes of the mechanical test: the reference material exhibits ductile failure, while all 3D-printed samples demonstrate predominantly brittle fracture, with a strong dependence on build orientation. Horizontal builds (B, D) achieve higher strength but fracture along interlayer regions with minimal plasticity, whereas vertical builds (C) are the weakest due to poor interlayer bonding.

4.1.2 Porosity evaluation

The porosity of individual 3D-printed samples was evaluated after printing, both perpendicular and parallel to the printing direction. As illustrated in Fig. 5 a), the porosity is depicted perpendicular to the printing direction, while Fig. 5 b) shows the porosity parallel to the printing direction. In these directions, porosity was measured at 0.41 % (perpendicular direction) and 2.09 % (horizontal direction). As illustrated in Fig. 5 b), the pores between the individual printed fibres (extruder trajectories) can be observed. The formation of pores can be attributed to various factors, including inadequate material extrusion during printing, an excess of binder in the input material, or insufficient energy supply during the sintering process. During the sintering process, metal particles require energy, which is measured in terms of both time and temperature, to bond with one another and to close the pores that are created following the removal of the binder. As illustrated in Fig. 5 c), the image displays the total porosity. The total porosity value was measured at 6.13 %, with a maximum pore size of 7.43 µm. The pores manifest in the interstices between the deposited layers. Consequently, these discolorations are not attributable to inadequate or deficient washing procedures. In such instances, the presence of pores can compromise the mechanical integrity of the component, often resulting in brittle

fracture. As demonstrated by Åsberg et al. [14] and Fryzowicz et al. [15], lower material porosity can be achieved through the utilisation of alternative additive methods. Åsberg et al. [14] achieved a part porosity of 0.07 ± 0.16 % in their study, and after HIP, they measured a porosity of 0.005 ± 0.001 %.

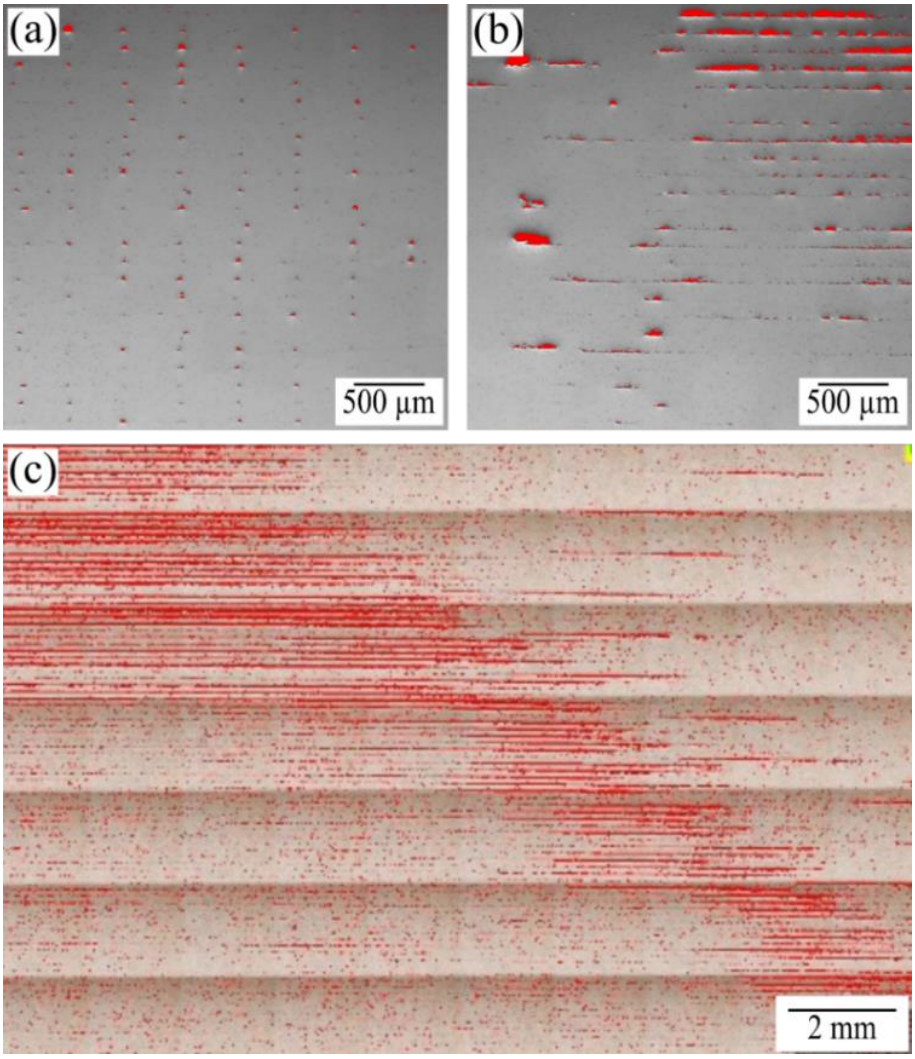

Fig. 5 Porosity evaluation
a) direction perpendicular to the direction of printing, b) direction parallel to the direction of printing, c) overall view of porosity in the direction perpendicular to the direction of printing

To achieve lower porosity, a second sintering process (II. sintering) was performed. It was expected that pore closure would require both heat and time, as the extended sintering duration allows more time for the powder material to melt completely and approach a fully molten state. The II. sintering process was conducted under the same conditions as the first sintering process (I. sintering).

However, increasing the sintering temperature or holding it for a longer time may lead to over aging [16], which can reduce tensile strength, increase elongation, and decrease hardness. Porosity was measured optically over an area of 292 mm², and the results showed an approximate 1.6 % reduction compared to the porosity before the II. sintering process. Tab. 4 shows a brief summary of measure porosity for AB and II. sintering samples.

Tab. 4 Porosity of AB samples and after II. sintering

	AB	II. sintering
Porosity (%)	6.13	4.53

4.1.3 AB samples for machining

Three metal test blocks (60 x 30 x 20 mm) were produced by material extrusion for the machinability test. Solid carbide end mills with a titanium nitride (TiN) coating were utilised for the machinability tests. These end mills should be capable of machining material up to a hardness of 60 HRC. In the sintered state, the printed samples exhibited a hardness of 47.5 ± 5 HRC. The machinability of a material is influenced by numerous parameters, including the workpiece material, the cutting conditions, clamping, cooling, etc. Tab. 5 lists the machining conditions that were constant during the tests. The tool wear was evaluated using a Zeiss Stemi 2000-C optical microscope.

Tab. 5 Parameters which were constant during the experiment

End mill diameter (mm)	Number of teeth (mm)	Depth of cut a_p (mm)	Radial depth of cut a_e (mm)	Type of milling (–)
3	4	0.2	2.4	Down milling

The primary objective of this investigation was to evaluate the influence of cutting conditions, cutting speed (v_c), feed per tooth (f_z), and type of cooling (DM – dry machining and FC – flood cooling) on the machinability of the samples. The experimental tests were conducted employing a full factorial design, in accordance with the DoE method. The individual measurement sequences were randomized. The experiment is illustrated in Tab. 6. The twelve tests, ranging from I to XII, encompass a range of methods including visualisation. Each of the printed samples was used for four machinability tests. The testing methodology is illustrated in Fig. 6 (a). The clamped sample is displayed in Fig. 6 (b).

Tab. 6 Individual tests prepared and visualized by the full factorial DoE

Test	v_c (m.min^{-1})	f_z (mm)	Cooling conditions	Sample
I	90	0.0075	FC	A
II	80	0.005	FC	
III	90	0.0075	DM	
IV	100	0.01	FC	
V	80	0.005	DM	B
VI	100	0.01	DM	
VII	90	0.0075	DM	
VIII	90	0.0075	FC	
IX	100	0.005	FC	C
X	100	0.005	DM	
XI	80	0.01	DM	
XII	80	0.01	FC	

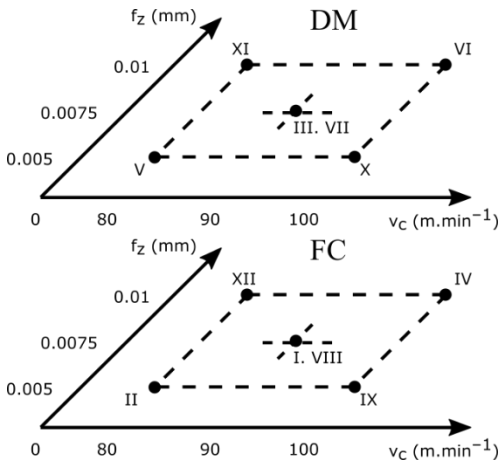

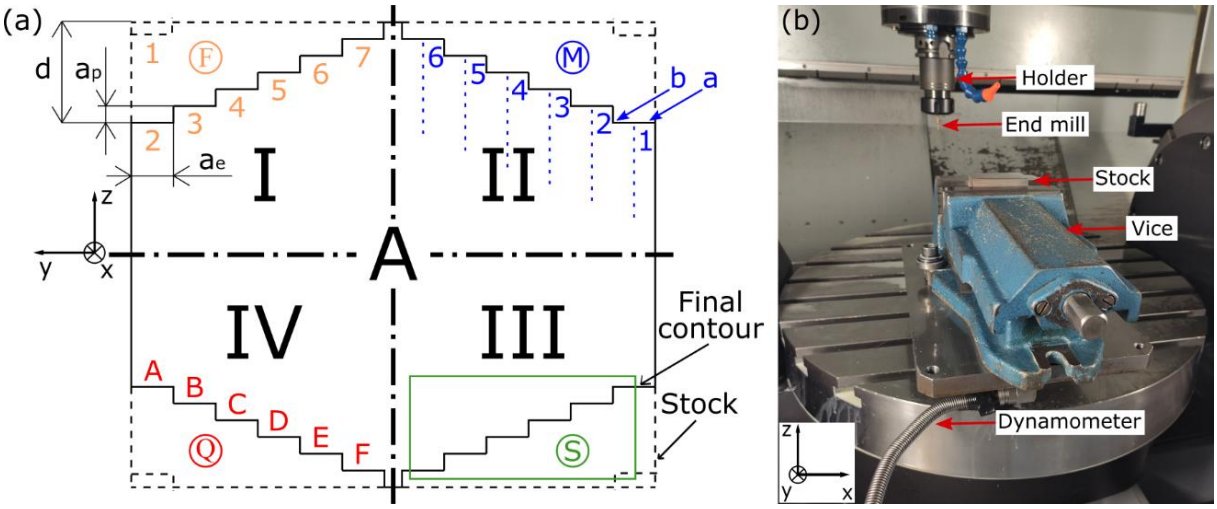

Fig. 6 a) Detail of the used methodology showing the areas of the forces measurement (F), microhardness evaluation (M), structure observation (S), and quality examination (Q). Each variable was evaluated for each test, b) the real setup of the experiment during the machinability tests.

Tests listed in Tab. 6 were subjected to cutting forces measurements (F), microhardness evaluation (M), structure observation (S), and quality examination (Q). The measured region where the analysis was done at each sample are depicted in Fig. 6 a).

The cutting forces (F) were measured in regions 1–7 using a Kistler dynamometer, which can measure forces in three perpendicular axes. The data were recorded at a frequency of 4 kHz and processed using Dynoware software. The duration of each test was different, but the cutting length remained the same. The total machine length for each test was 3.420 mm. Fig. 6 a) shows quadrant I. This section shows area number 1, which identifies the beginning of the test. Number 7 in quadrant I then indicates where the test ends. The microhardness (M) of the samples was measured in accordance with the methodology delineated in Fig. 6 a). In order to examine microhardness, the sample was cut perpendicularly, and microhardness was examined at various depths according to the lines shown in the schematic representation in quadrant II of Fig. 6 a). The microhardness measurement was performed on the LECO 247 (INNOVATEST, Prague, Czech Republic) device in an as-built state using a 50 g load, with a dwell time set to 10 s. The structure of the material was observed on a sample according to the methodology described in Fig. 6 a) in region III. The structure was observed using an Olympus DSX 500 optical microscope. The samples for structure observation were prepared after machining by puck casting, automatic polishing, and etching with 2% nital. For studying the microstructure, Tescan Lyra 3 with EBSD detector was used. The scanning step for EBSD (electron-backscatter) was set to 0.19 µm. Surface quality was analyzed according to methodology shown in Fig. 6 a) region IV at areas A to F. Average surface roughness (Ra) was evaluated in each of that area using T4 contour graph device. Further observation of surface was done with Alicona Infinite Focus G5 digital device and KEYENCE VHX F microscope. The surface layer was examined regarding residual stresses with XRD.

As demonstrated in Fig. 7, the surface roughness was evaluated using a KEYENCE digital microscope. The surface quality, in its as-built state, exhibited a Ra value of 6.45 µm and a Rz value of 24.3 µm. It is evident that these values do not align with the established industry standards [17]. Consequently, the implementation of post-processing milling machinery is imperative to ensure conformity and optimise outcomes.

As illustrated in Fig. 7 a), a visible crack is evident on the uppermost surface of the as-built samples, indicated by the red arrow. The root cause of this issue is the non-alignment between the deposited feedstock in this area and the applied printing strategy. As illustrated in

Fig. 7 b), the presence of nozzle cladding is evident, along with the layer thickness of the samples. As demonstrated in Fig. 7 c), there is also a visible presence of pores, indicated by yellow arrows. As displayed in Fig. 7 d), the surface roughness is depicted by the Rz parameter. Consequently, the samples were subjected to subtractive machining to prepare them for the subsequent machinability tests.

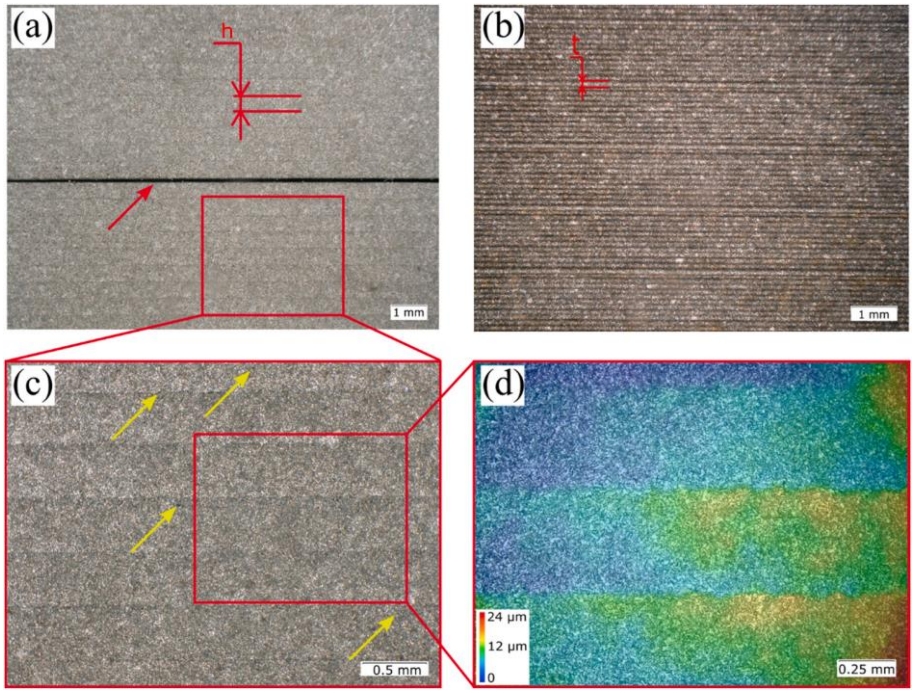

Fig. 7 a) top surface of printed samples, b) side view of printed samples, c) area of interest and d) Rz surface roughness analysis

4.1.4 Cutting forces evaluation

This section of the thesis undertakes an evaluation of the individual components of the cutting force F_c, i.e. F_x, F_y, and F_z. The maximum recorded value was observed for the force F_y. The testing was carried out in accordance with the parameters delineated in Tab. 6. The data was recorded using the Dynoware program, which was also used to calculate the average force. The values were subsequently exported and underwent further processing. The calculated values are presented as mean values related to the individual areas of the individual tests.

The dependence of the average forces F_x, F_y, and F_z on the cutting length with and without cooling is demonstrated in Fig. 8. The primary force (exhibiting the highest measured values) is measured along the Y-axis, which corresponds to the direction of the milling cutter feed. The lowest cutting force values were measured in the Z-axis (vertical direction), which correlates with the passive force generated during machining. The values were interpolated with a regression curve, which exhibited an upward trend (the forces increased with increasing machined length) in the case of machining with process fluid. In the absence of process fluid during machining operations, these forces exhibit consistent and predictable values. No significant deviation was observed in any of the tests, with the exception of test IV, where the deviation was found to be at its greatest. This test was conducted under highest cutting conditions with cooling. As demonstrated in test XII, the regression curve demonstrates the most significant degree of growth. The observed difference between the first and last measurements in this instance was 73.3 N, which corresponded to the maximum recorded variation. The observed difference may be attributed to the lowest cutting conditions and, consequently, the longest engagement time. At the beginning of the present test, the F_y force value was the lowest in comparison to the other tests; however, at the conclusion of the

experiment, it reached values that were similar to those in tests IV and VIII (which were performed at higher cutting speeds and feed rates per tooth).

To facilitate optimal visualization, the graphs below have been divided into two categories: machining without cooling (Fig. 8 b), e) and f)) and machining with cooling (Fig. 8 a), c) and e)). The difference between machining with and without cooling is clearly visible. An upward trend in cutting forces has been observed in the context of cooling, while stable cutting forces have been noted in the domain of so-called dry machining. In tests conducted without the utilization of cooling mechanisms, reduced cutting forces were observed at cutting speeds of 90 $m.min^{-1}$ and 80 $m.min^{-1}$ when compared to tests performed under analogous conditions with the incorporation of cooling mechanisms. The highest forces were measured in test IV. In general, higher cutting speeds have been shown to generate lower forces [18], a finding that was also confirmed in test IX. In this test, the cutting speed was set at 100 $m.min^{-1}$ and the cutting force F_y achieved the lowest recorded value. It was demonstrated that the magnitude of the cutting forces was reduced by both the cutting speed and the lower feed rate per tooth (0.005 mm). When a higher load is applied to the milling cutter due to an increased feed rate per tooth, the wear of the cutting edge (VB) accelerates, which in turn leads to an increase in cutting forces. Furthermore, an increase in cutting forces has been shown to result in an enhancement of surface roughness [19]. Milling is characterized by an interrupted cut, which can be described as a load period (in the cut) followed by a no-load period (outside the cut). This factor has a detrimental effect on the overall tool life. Tool life can be reduced by thermal shocks, defined as sudden changes in temperature. It has been demonstrated that exposure to thermal shocks can result in greater degradation of cutting tools when compared with exposure to high temperatures in the absence of thermal shocks [20]. It has been demonstrated that tools which are engaged for a sustained period do not experience thermal shocks [21]. It has been established that exposure to thermal shocks, which increase with increasing cutting speed, can result in thermal fatigue. This, in turn, can lead to the formation of thermal cracks [22]. Friction is defined as the resistance experienced when one body moves relative to another. In this context, it occurs at the point of contact between the cutting tool and the workpiece, causing an increase in temperature. Following the completion of the incision and the subsequent fracture of the chip from the workpiece, the area undergoes a cooling process. This is then followed by the occurrence of additional friction, which arises from the repeated contact between the cutting tool and the workpiece. The impact of cooling was manifestly evident during the experimental procedure. In the absence of cooling during machining operations, the cutting forces exhibited stability, consequently leading to enhanced surface quality (Ra parameter) and reduced tool wear (VB).

The resultant force exerted by each test was calculated and is displayed in Fig. 9. The figure indicates a marked increase in total force with increasing distance in the stroke when tests are performed with cooling. Conversely, tests conducted without the use of cooling mechanisms demonstrate a slow and steady rise in total force.

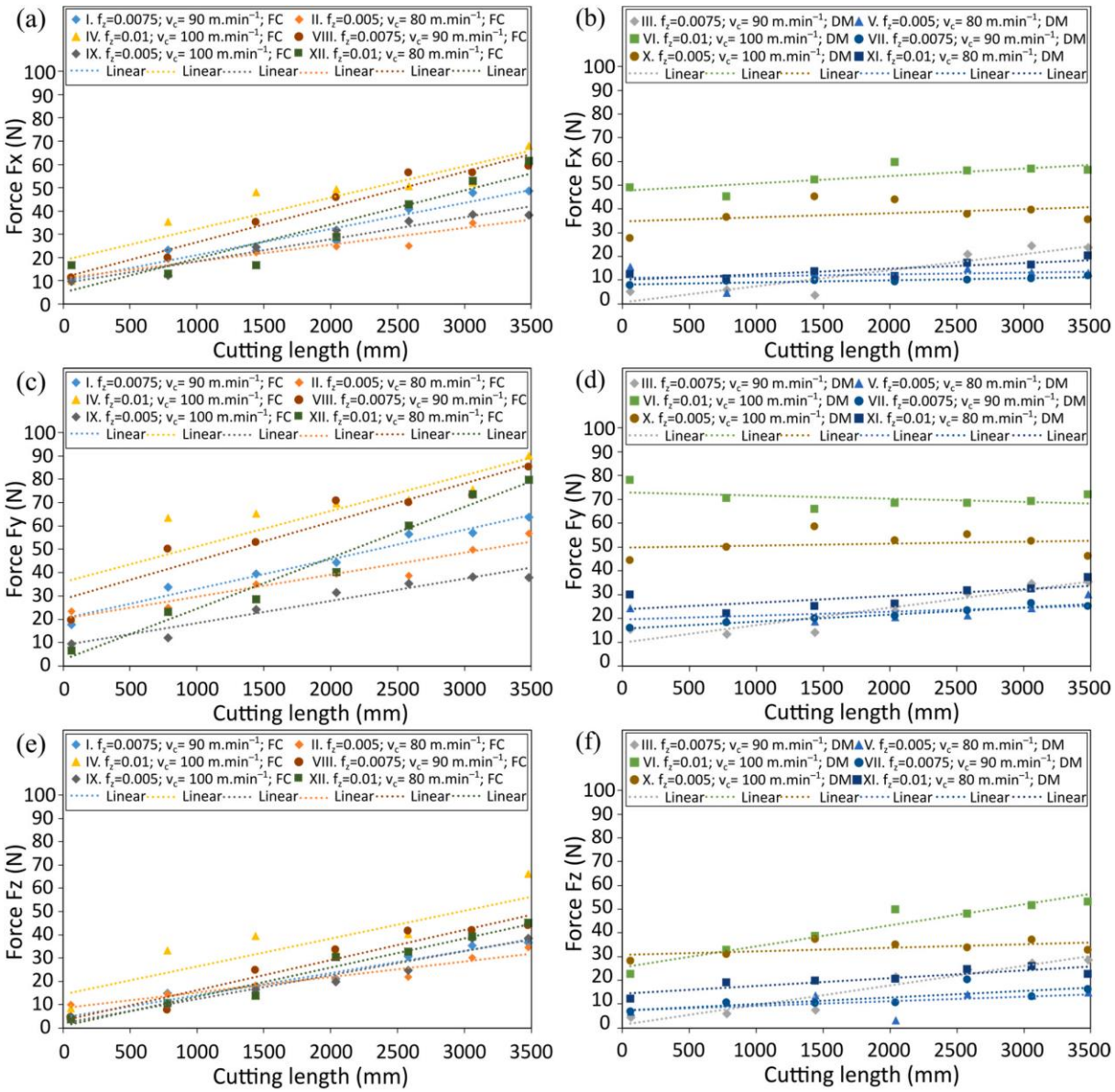

Fig. 8 Dependence of the average F_x, F_y, and F_z forces on cutting length, a) F_x force under the FC, b) F_x force under the DM, c) F_y force under the FC, d) F_y force under the DM, e) F_z force under the FC, f) F_z force under the DM

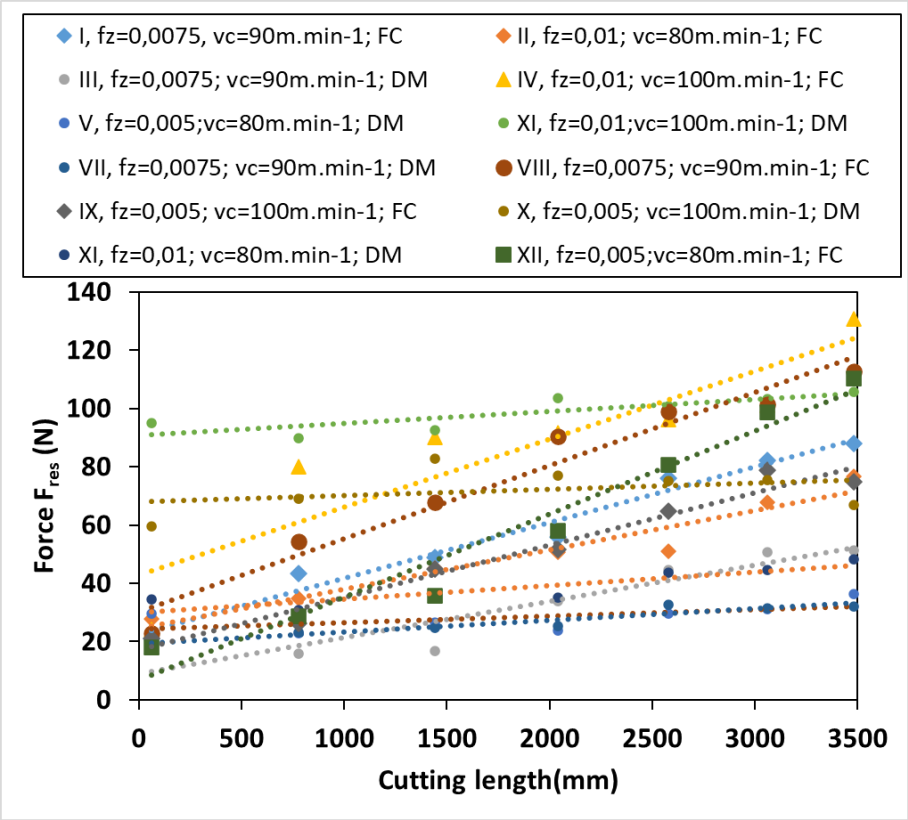

Fig. 9 Dependence of the average F_{res} on cutting length

4.1.5 Machined surface quality evaluation

The average surface roughness, characterized by the Ra parameter, was evaluated as described in Fig. 6 a). Fig. 10 illustrates the influence of cutting length on Ra. Specifically, Fig. 10 a) presents tests in which Ra exhibited either a stable or decreasing trend with increasing cutting length, whereas Fig. 10 b) shows tests characterized by increasing surface roughness, primarily toward the end of the cutting length. In all cases, dry machining (DM) showed lower surface roughness compared to flood cooling (FC).

Upon data analysis, it was observed that an increasing feed per tooth (f_z) generally led to higher surface roughness, consistent with findings reported by Oliveira et al. [23] and Liao et al. [24]. However, in Test VII, conducted under intermediate cutting conditions (cutting speed $v_c = 90$ m·min^{-1}, feed per tooth $f_z = 0.0075$ mm), surface roughness reached a minimum value of 0.08 µm. In summary, the surface roughness is influenced by the feed per tooth and the type of cooling, since the cutting speed resulted in very similar Ra values in tests with the same f_z and FC. The highest surface roughness, measured at 0.13 µm, occurred under FC conditions in test IV. Lower cutting speeds were generally associated with reduced surface roughness.

The surface texture was further examined in Test VII, which exhibited the lowest Ra value. Fig. 11 a) provides a top-view scan of the cutting lengths, while Fig. 11 b) details individual tool paths (A to F). The formation and accumulation of burrs along the edge increased with cutting length; the most prominent burrs, observed at track F, are marked with yellow arrows, with additional detail shown in the SEM image. A greater tendency for burr formation was correlated with tool wear (VB) evolution, consistent with conclusions drawn by Aslantas and Alatrushi [25]. As VB progressed, chip formation deteriorated, especially along the edge of the cutting length.

The experiments employed down milling, which is known to produce wider burrs compared to up milling due to its cutting mechanics [26]. Fig. 11 c) illustrates the tool lead-out region, where

induced oscillations, highlighted in blue, were observed. A direct relationship was found between increased cutting speed and vibration amplitude, which can contribute to elevated surface roughness [27]. In contrast, lower cutting forces, as recorded in Test VII, are associated with reduced elastoplastic deformation during machining, which positively influences the resulting surface quality [28].

Finally, Fig. 11 d) presents a detailed image of the milled surface texture, aligned with varying feed per tooth values. Notably, adhered chips are visible and highlighted with black arrows, indicating material transfer during cutting.

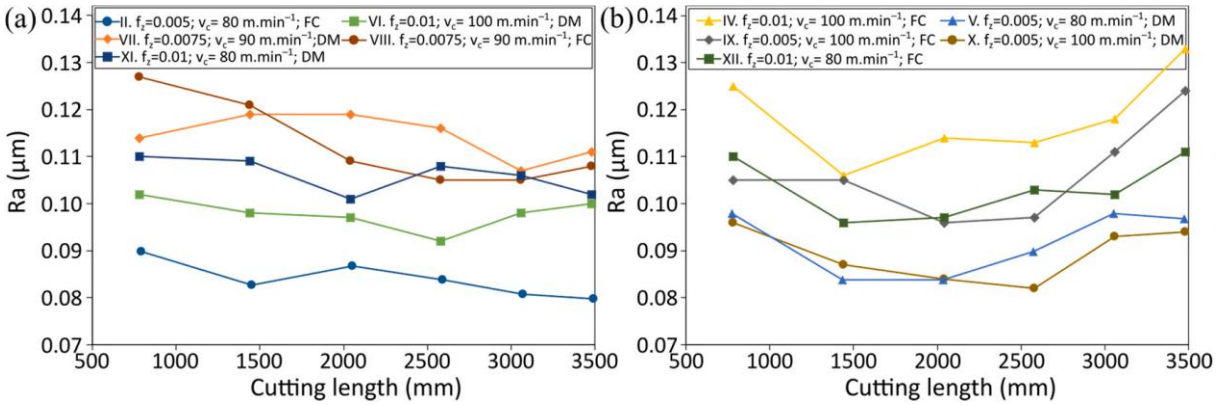

Fig. 10 Surface quality represented with average surface roughness parameter Ra in connection with the cutting lengths depicted for different tests, a) tests II, V, VI, VIII, and XI and b) tests IV, VII, IX, X, XII

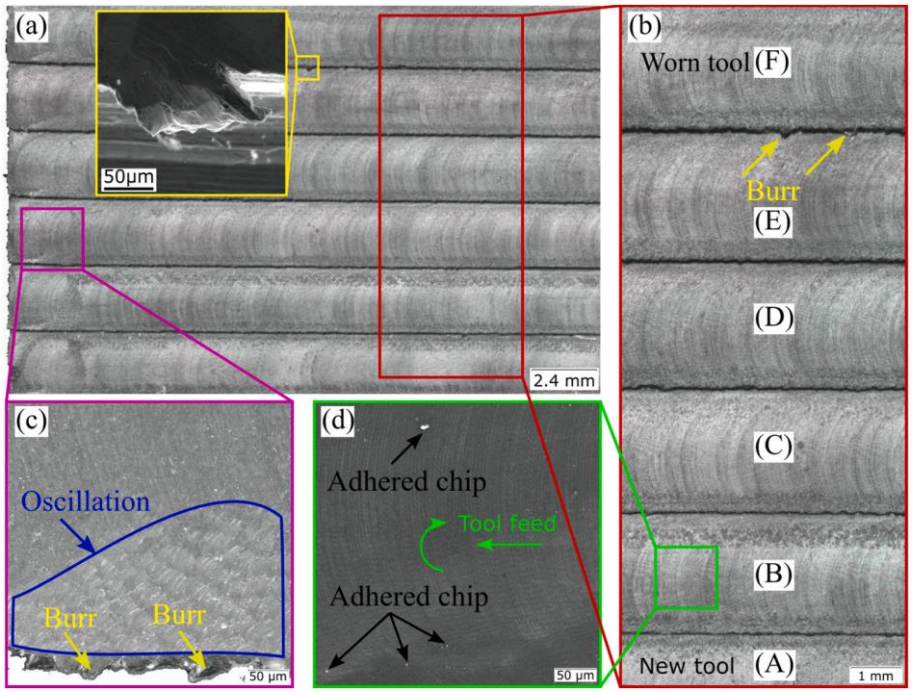

Fig. 11 Surface texture obtained in test VII: a) scan of the cutting lengths, b) detail of the individual tracks A to F, c) the detail of the induced oscillation during the lead out of the tool, and d) the detail of the surface texture depicting the milling traces corresponding with the feed per tooth.

4.1.6 Structure observation

Optical microscopy, specifically the utilisation of light optical microscopy (LOM), was performed on a transverse cross-section of sample B, consistent with the orientation presented

in Fig. 6 a). The specimen was prepared with the cross-section oriented perpendicularly to the machined paths and parallel to the building direction. The LOM images (Fig. 12) clearly demonstrated the presence of a distinct hardened layer, indicated by red arrows in Fig. 12 a), located immediately beneath the machined surface. The formation of this layer is directly correlated with the observed alteration of the surface microhardness. Quantitative analysis determined the width of this hardened layer to be approximately 20 µm, a dimension that notably exceeds the values reported for machined additively manufactured Ti6Al4V alloy [29]. Furthermore, the microstructural analysis demonstrated the widespread presence of numerous pores throughout the material (see Fig. 12 b) and c)), which are characteristic of the sintering process. As is well documented in the extant literature, the effectiveness of sintering temperatures in reducing porosity is well-established, with the concomitant increase in material density being a well-documented phenomenon [30]. Alternatively, the implementation of reduced layer thickness parameters during the additive manufacturing process has been shown to be an effective means of mitigating porosity [31]. Within the observed microstructure, prior austenite grains (PAGs) were clearly discernible (Fig. 12 d), delineated by blue lines), with their boundaries exhibiting a pronounced differential etching contrast when compared to the bulk of the grain interiors.

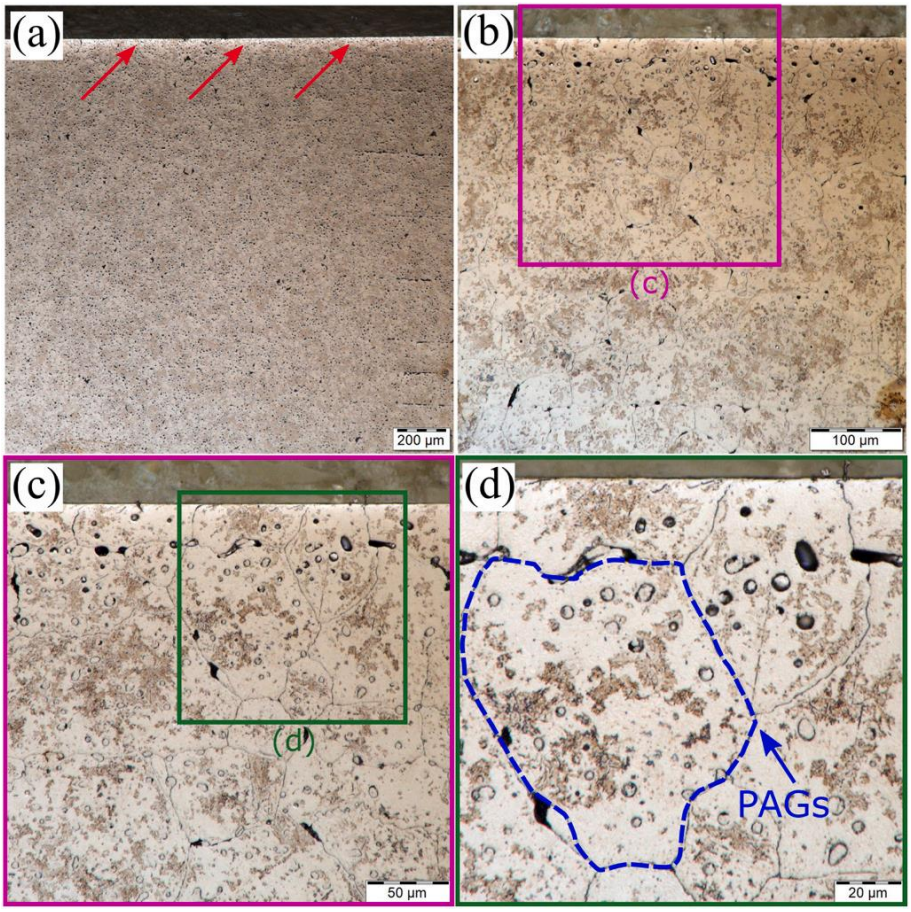

Fig. 12 Structure of H13 TS depicted directly after the machining process, a) macro image showing a hardened surface layer, b) & c) areas of interest, and d) detail of structure with visible PAGs.

4.2 Machining of samples after heat treatment

Samples for machinability analysis after heat treatment were produced using an additive material extrusion method. Two test blocks measuring 60 x 30 x 20 mm were produced. The third sample corresponded to a conventionally produced (rolled) block of equivalent dimensions.

The samples that underwent heat treatment were first heated to a temperature of 1035 °C at a heating rate of 222 °C/h and held at that temperature for 35 minutes. The process was conducted within an argon atmosphere, which is known to provide a protective barrier against potential damage or contamination. Subsequently, the samples underwent air-hardening and tempering processes, each cycle comprising two distinct phases. The initial tempering process was conducted at a temperature of 600 °C for a duration of 4 hours, while the subsequent tempering stage was executed at a temperature of 575 °C for an equal duration of 4 hours. Both cooling processes took place in air until the temperature of the system was equal to the ambient temperature.

A total of three types of samples were tested: as-built (AB), heat-treated additively manufactured (HTAM), and heat-treated wrought (HTW). The machinability evaluation was performed using solid carbide end mills coated with TiN. These milling cutters are engineered for milling materials with a hardness of up to 60 HRC. The milling parameters, which remained constant throughout the measurement process, are listed in Tab. 7.

The primary objective of this study was to evaluate the influence of cutting conditions (cutting speed, feed per tooth, and type of cooling) on the machinability of the material.

Tab. 7 Constant milling parameters

End mill diameter (mm)	Number of teeth (mm)	Depth of cut a_p (mm)	Radial depth of cut a_e (mm)	Type of milling (–)
8	4	0.2	8	Slot milling

The study procedure is outlined in Tab. 8, which includes 12 tests (I-XII) with specific cutting conditions. The right-hand side of the table provides a visualisation of the experiment planning with regard to cutting conditions. The cutting conditions were selected in accordance with the tool manufacturer's recommendations. For each of the samples (AB, HTAM, HTW), a series of 12 machinability tests were conducted. Each test was performed three times to increase the amount of relevant data. The testing methodology is illustrated in Fig. 13 a), and the evaluation of the samples is schematically demonstrated in Fig. 13 b).

Tab. 8 Tests performed for samples AB, HTAM and HTW

Test	v_c (m.min^{-1})	f_z (mm)	Cooling conditions	Sample
I	40	0.02	DM	
II	80	0.02	DM	
III	60	0.03	DM	
IV	60	0.03	DM	
V	40	0.04	DM	
VI	80	0.04	DM	AB, HTAM, HTW
VII	40	0.02	FC	
VIII	80	0.02	FC	
IX	60	0.03	FC	
X	60	0.03	FC	
XI	40	0.04	FC	
XII	80	0.04	FC	

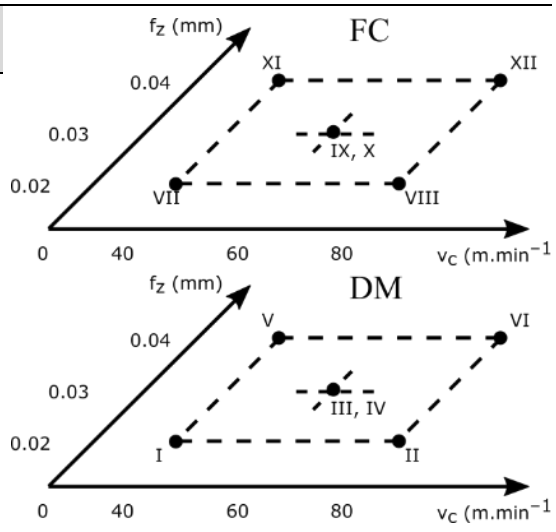

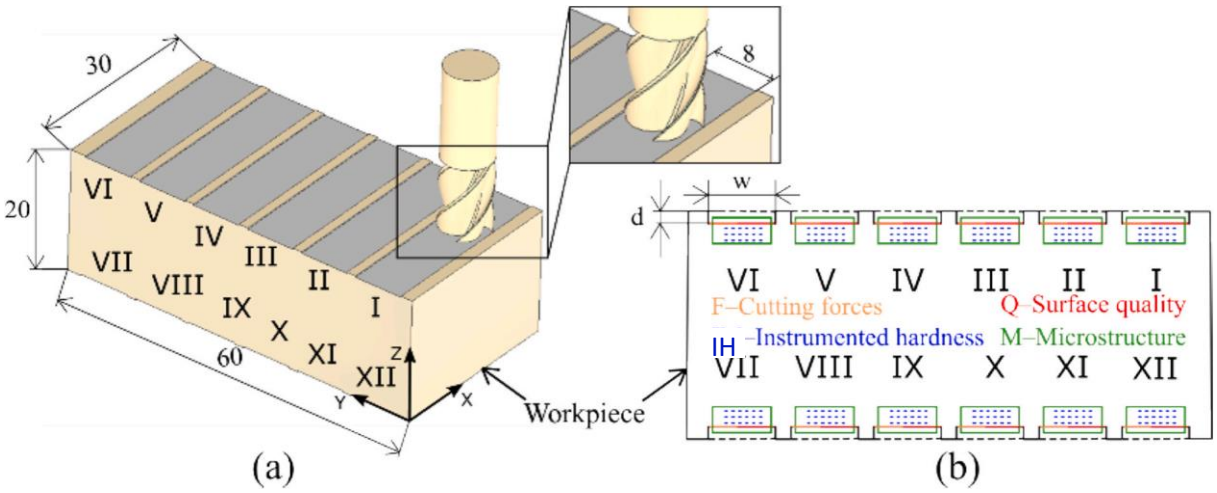

Fig. 13 a) Setup of experiment during machinability tests, b) detail of used methodology showing the areas of the forces (F) and microhardness (M) measurements, structure (S) observation and surface quality (Q) examination.

4.2.1 MEX manufactured sample hardness and structure characterization

Porosity measurements were performed on all three types of samples. The lowest recorded value was observed in the HTW sample, with a measurement of 0.07 ± 0.04 %. Samples produced using MEX achieved significantly higher values. AB samples achieved a porosity of 4.83 ± 0.95 %. In the case of HTAM samples, the porosity value was found to be 2.63 ± 0.67 %. It is evident that the application of heat treatment resulted in the anticipated reduction in porosity. It is important to note that lower porosity values can be achieved with other 3D printing technologies.

Fonseca et al. [32] achieved a porosity of 0.05 ± 0.02 % with PBF, and Åsberg et al. [14] achieved a porosity of 0.07 ± 0.16 %. Lower porosity is achieved thanks to the selected printing technology.

Consequently, a Computed Tomography (CT) scan (see Fig. 14) was performed to verify the porosity results derived from optical observation. The HTW sample achieved a porosity of 0.06 %, the AB sample 4.76 %, and the HTAM sample 1.87 %. It can be stated that porosity measurement using CT scanning yielded similar results to optical porosity assessment for the HTW and AB samples. However, it has been demonstrated that optical porosity measurement is significantly reliant on the particular sample under investigation, as evidenced by the variation in porosity values measured for the HTAM sample.

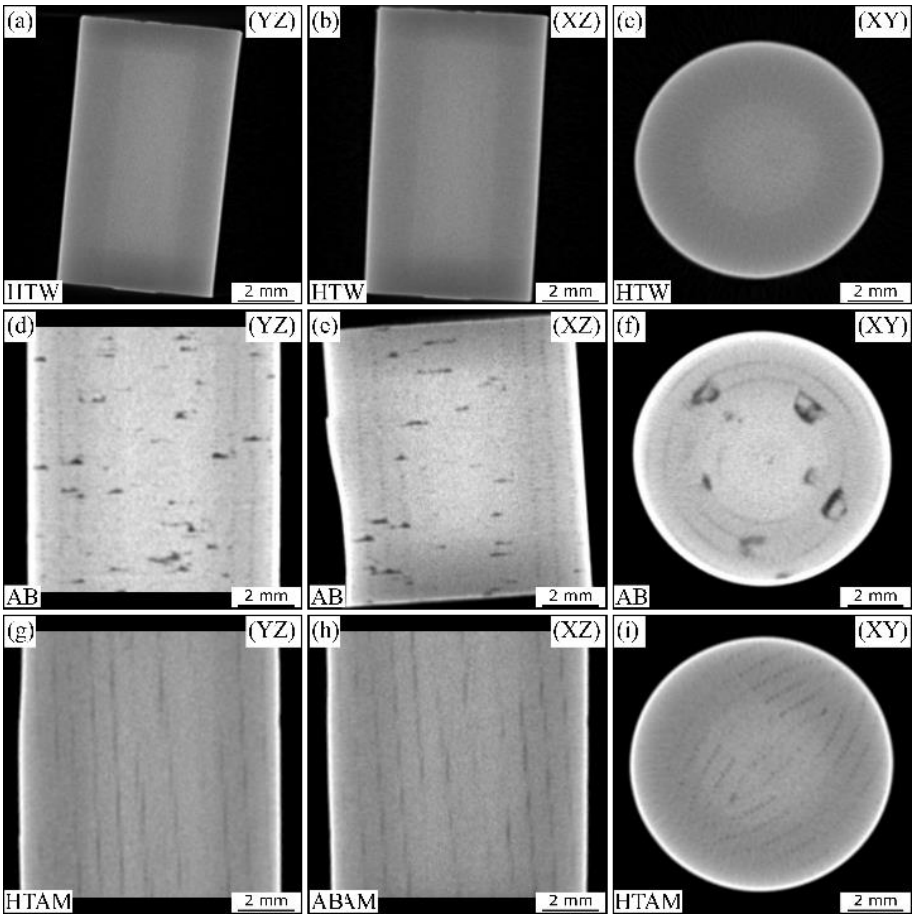

Fig. 14 Micro CT porosity measurement for HTW sample (a–c), AB sample (d–f) and HTAM sample (g–i)

The AB sample demonstrated a hardness of 33.2 ± 3.0 and 31.9 ± 3.0 HRC in the horizontal (XY) and vertical (YZ) directions, respectively. The hardness of the HTAM sample was found to be 40.6 ± 2 HRC and 38.4 ± 2 HRC, respectively. The application of used heat treatment resulted in an enhancement of the hardness of the AM samples. The hardness of the HTW samples was found to be 47.8 ± 3.0 and 46.4 ± 3.0 HRC.

Tool wear (TW) was analysed using electron microscopy at the conclusion of each cutting test series. In order to eliminate the potential for damage caused by tool wear, a new endmill was used for each cutting test. As illustrated in Fig. 15 b), the top view of the endmill is presented, while Fig. 15 a) and c) offer close-up views of the tool tip following testing. The TW is observable at the cutting tip, with its maximal values reaching 0.07 mm (measured as the distance between the tool edge and the point at which tool wear extended) at the conclusion of the cutting test in the case of the HTW sample. It is evident from the analysis of the AB and HTAM samples that the TW attained values of 0.04 mm and 0.06 mm, respectively. These variations were attributed primarily to the differences in initial material hardness associated with each material type and post-processing via heat treatment. The micro-chipping wear mechanism of the cutting edge was observed in the AB sample due to the existence of pores within the material structure, which manifested as multiple interrupted cuts during the individual cutting edge revolution. Conversely, the elevated position of the harness in the HTAM and HTW models primarily resulted in an abrasive wear mechanism. Nevertheless, analogous wear characteristics were observed across all cutting tests. Consequently, the data indicated comparable cutting performance across additively manufactured tested material variants, regardless of whether they were produced via additive manufacturing or conventional (rolled) processes. Furthermore, it can be concluded that the tool wear mechanism underwent

a change following the heat treatment, attributable to a substantial reduction in residual porosity and an increase in material hardness.

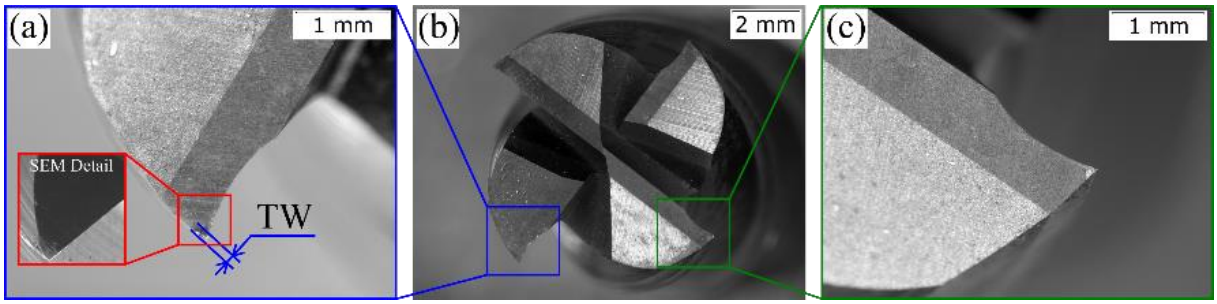

Fig. 15 Used end mill: a) area of interest, b) overview of the end mill and c) detail of the cutting tip.

4.2.2 Cutting forces measurements

The study under discussion addresses the importance of measuring cutting forces as a key indicator of material machinability. The cutting forces, that is to say F_x, F_y and F_z, were evaluated in three perpendicular axes, corresponding with the testing methodology illustrated in Fig. 13 a). Specifically, F_x denotes the cutting force, F_y represents the feed force, and F_z refers to the passive force. The forces were recorded using Dynoware software, which also calculated mean values to streamline data analysis. This approach effectively minimised common measurement errors, such as noise. Consequently, mean force values are presented for each cutting test (I–XII). The result force (F_{res}) was calculated from the three cutting forces. As illustrated in Fig. 16, there is a clear variation in the mean forces (F_{res}) across all cutting conditions. The cutting force F_x demonstrated the highest observed value across all the samples that were tested, while the lowest forces were recorded in the Z-axis. It was evident that the force F_x exhibited an increasing tendency with elevated cutting conditions, as evidenced by the AB and HTAM samples. With regard to the HTW sample, a comparable tendency was observed; however, a difference was noted in the tests conducted at the same feed rate. In this instance, the AB and HTAM samples demonstrated an increase in cutting force F_x with an increase in cutting speed. However, the HTW sample exhibited a reverse trend. The phenomenon can be explained by a material softening effect caused by higher heat generation during the higher cutting speeds, as described in [33; 34]. The heat-treated HTW and HTAM samples exhibited elevated cutting force F_{res} in comparison to the AB sample. A comprehensive analysis of the collected data reveals that HTW exhibits superior machinability when compared with HTAM. However, under the lowest cutting conditions (tests I and VII), the HTAM sample demonstrated lower cutting forces (by 23.7 % in dry machining and 24.5 % under flood cooling) compared to HTW.

The utilisation of FC is dependent upon its capacity to reach the cutting zone, which is a primary factor in determining its effectiveness. In high-speed or deep-cut operations, the fluid may not penetrate efficiently due to the formation of vapor barriers or centrifugal forces ejecting the fluid away from the tool–workpiece interface [35]. Consequently, the intended benefits of cooling and lubrication are diminished, which may result in performance levels comparable to those of dry machining. This assertion is confirmed by the findings of the study. In the lower cutting speed tests (tests I and VII), the flood cooling exhibited superior performance in terms of cutting forces. Conversely, elevated cutting conditions gave rise to analogous or augmented cutting forces in instances of flood cooling. Secondly, a number of studies have demonstrated that, under specific conditions, dry machining can yield results that are competitive or even superior. To illustrate this point, consider the machining of hardened steels. It has been demonstrated that dry conditions may reduce thermal shock and maintain tool integrity more effectively than conventional flood cooling methods [36]. Furthermore, the tool material and

coating, the workpiece material, the cutting parameters, and chip formation dynamics also influence the effectiveness of cooling methods. In instances where contemporary tool coatings such as TiAlN or AlCrN are employed, which are engineered to endure elevated temperatures, the merits of flood cooling may be negligible, as asserted by Soham et al. [37].

Therefore, while it might be anticipated that FC would demonstrate superior performance in comparison to DM according to conventional assumptions, the extant literature indicates that, under specific machining conditions and configurations, dry machining may exhibit a comparable level of performance.

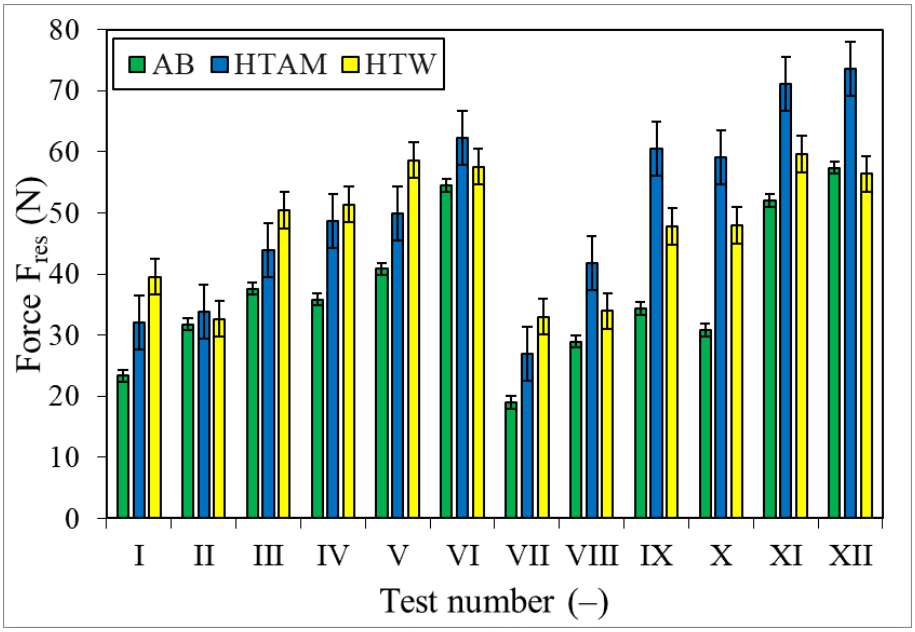

I. f_z=0.02; v_c= 40 m.min^{-1}; DM
II. f_z=0.02; v_c= 80 m.min^{-1}; DM
III. f_z=0.03; v_c= 60 m.min^{-1}; DM
IV. f_z=0.03; v_c= 60 m.min^{-1}; DM
V. f_z=0.04; v_c= 40 m.min^{-1}; DM
VI. f_z=0.04; v_c= 80 m.min^{-1}; DM
VII. f_z=0.02; v_c= 40 m.min^{-1}; FC
VIII. f_z=0.02; v_c= 80 m.min^{-1}; FC
IX. f_z=0.03; v_c= 60 m.min^{-1}; FC
X. f_z=0.03; v_c= 60 m.min^{-1}; FC
XI. f_z=0.04; v_c= 40 m.min^{-1}; FC
XII. f_z=0.04; v_c= 80 m.min^{-1}; FC

Fig. 16 Average total force F_{res} corresponding to cutting tests with noticeable cutting conditions corresponding to individual test.

4.3 Influence of the printing direction on the machining direction

The aim of this analysis was to verify the effect of the direction of application of individual printed layers on the resulting machinability of the material. When printing layer by layer, the material does not develop homogeneous properties in all directions. The individual machining directions depending on the direction of the part's print are illustrated in Fig. 17.

The perpendicular direction is characterized by the fact that the machining direction is perpendicular to the direction of material deposition in additively manufactured samples, while in conventionally manufactured samples it is perpendicular to the rolling direction (see. Fig. 17 b)).

The longitudinal direction means that machining takes place in the direction of material deposition for additively printed samples or in the direction of rolling for conventionally manufactured samples (see Fig. 17 a)). The vertical method is again performed perpendicular

to the direction of material deposition or rolling, but the sample is placed in a vertical position, as can be seen in Fig. 17 c).

Nine types of samples were produced for the experiment itself. Three samples were in as-built (AB) condition, three samples were printed with heat treatment (HTAM), and three samples were produced conventionally with heat treatment (HTW).

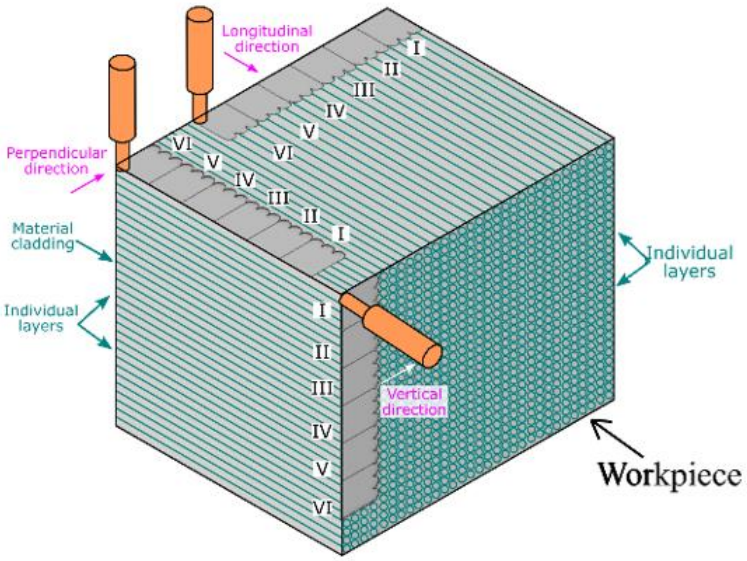

Fig. 17 Illustration of the machining direction in relation to the printing direction, numbers I–VI represent individual tests

The aim of the experiment was to evaluate the influence of the machining direction on the resulting cutting force, surface roughness, and tool wear. These phenomena were observed in relation to the machined material, machining direction, and cutting conditions. The cutting conditions were selected according to the milling cutter manufacturer's recommendations and are listed in Tab. 9.

Tab. 9 Machining conditions of each test

Test	v_c (m.min^{-1})	f_z (mm)	Cooling conditions	Sample
I	40	0.01	DM	AB, HTAM, HTW
II	110	0.01	DM	
III	110	0.02	DM	
IV	40	0.02	DM	
V	75	0.015	DM	
VI	75	0.015	DM	

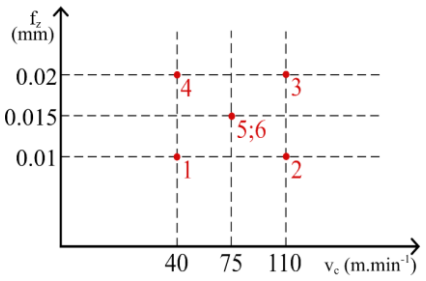

The parameters that remained constant during milling are shown in Tab. 1. The machining length was 7 mm. The samples were prepared and processed in the same way as it is described in case of 3rd sample series (Chapter 4.2).

Tab. 1 Constant milling parameters

End mill diameter (mm)	Number of teeth (mm)	Depth of cut a_p (mm)	Radial depth of cut a_e (mm)	Type of milling (–)
3	4	0.2	2.4	Down milling

4.3.1 Cutting forces analysis

Fig. 18 shows the force load during machining. The greatest difference in machining direction was observed in the as-built sample. Conversely, the HTW sample shows the least difference in the effect of the machining direction on the printing direction.

When machining the AB sample in the longitudinal direction, the tool encounters the greatest resistance. When machining perpendicular and vertical, pores in these areas reduce the material's resistance. These gaps are clearly visible in the chapter describing the material's structure. Due to the non-cohesive nature of the material, the force load on the tool is reduced. A further reason why greater forces are involved in longitudinal machining is that layers of material are cut at the joint where the material is harder (at the point where the caterpillars join). This can cause vibrations, increase forces, and reduce tool life. Discontinuous chips have been shown to exhibit substandard contact with the tool, thereby resulting in diminished heat dissipation at the chip-tool interface. This can result in localised overheating of the surface, increased wear, and the formation of microcracks.

In the case of the HTAM sample, these pores are smaller, resulting in lower differences in cutting forces between the individual machining methods (see Fig. 18. b)).

In the case of the HTW sample, heat treatment resulted in the recrystallisation of the material structure. Consequently, the rolling direction is not apparent, nor is the influence of the machining direction on the rolling direction of the material (see Fig. 18 c)).

Regarding the magnitude of the cutting forces in relation to the machining conditions, it was confirmed that the highest cutting forces are achieved with the highest feed per tooth and the lowest cutting speed (v_c = 40 m.min^{-1} and f_z = 0.02 mm). A higher feed per tooth increases the chip cross-section, which corresponds to an increase in force load. Lower cutting forces at higher cutting speeds may be caused by greater heat at the cutting point, softening of the material and reduced forces. Tests 5 and 6 were performed under the same cutting conditions, reaching similar cutting force values. Therefore, it can be concluded that machining was unaffected by phenomena such as tool and workpiece rigidity and clamping.

In terms of the comparison of cutting forces between the samples, it is evident that the AB sample exhibited the greatest cutting force. The HTAM and HW samples were heat treated to remove residual stress, which can reduce cutting forces.

It is evident that the feed per tooth is considerably smaller than the pore size of the material (0.1–1 mm). Consequently, the cutting edge repeatedly encounters voids rather than a continuous surface. This phenomenon gives rise to unstable cutting forces, intermittent chip formation, and localized impacts on the tool. Consequently, the surface quality deteriorates, chip formation becomes irregular and segmented, and tool wear accelerates due to repeated mechanical shocks and varying material resistance.

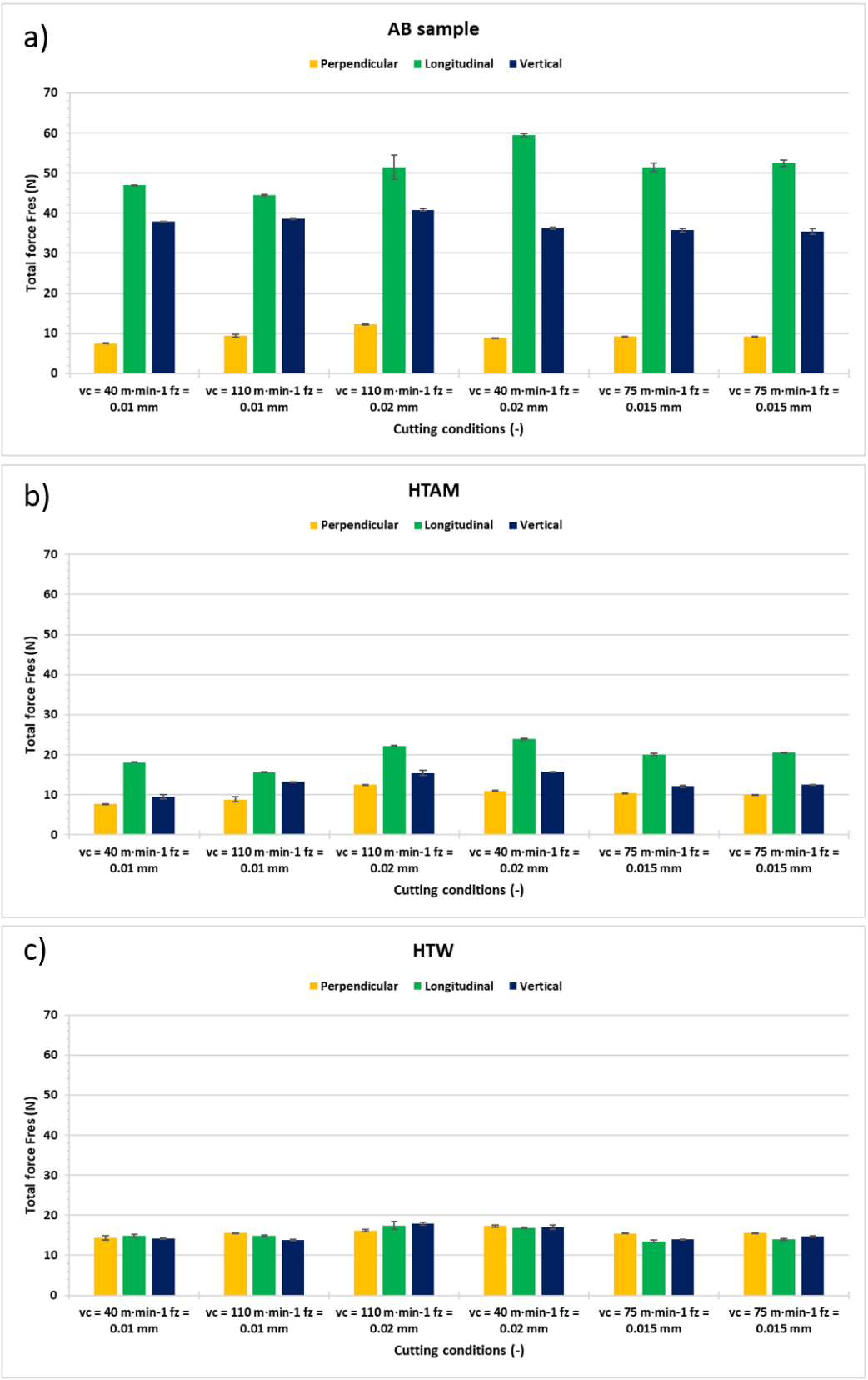

Fig. 18 Influence of cutting condition on cutting forces a) AB sample, b) HTAM sample and c) HTW sample

4.4 HIP + Heat Treatment of samples

Following a detailed evaluation of both experimental data and published studies, it was established that the application of hot isostatic pressing (HIP) significantly improves the mechanical properties of additively manufactured steel.

For this study, five categories of specimens were prepared. The first group comprised conventionally manufactured, rolled steel subjected to heat treatment (REF + HT). The second group consisted of additively manufactured specimens subjected to heat treatment (AB + HT). The third group included additively manufactured block-shaped specimens treated by HIP and subsequently heat treated (HIP REC + HT). The fourth group comprised additively manufactured bone-shaped specimens treated by HIP and subsequently heat treated (HIP BONE + HT). The fifth group underwent HIPping and was left without further HT (HIP). All specimens underwent identical heat treatment conditions. Furthermore, additional samples were examined immediately following the hiping process, i.e. without undergoing subsequent heat treatment.

The conditions for heat treatment and HIPing of samples are specified in the chapter on "Technologies and Measurement Instruments".

4.4.1 Tensile testing

Tensile tests performed on samples of H13 tool steel showed significant differences depending on the production technology used and subsequent heat treatment. The Fig. 19 shows mechanical properties of tested samples. Fig. 19 a) shows yield strength, b) ultimate tensile strength and c) ductility. The highest values of yield strength (YS ~1550 MPa) and ultimate tensile strength (UTS ~2000 MPa) were achieved in samples prepared by hot isostatic pressing (HIP – red colour). However, these samples were characterized by extremely low ductility (~2 %), which from a practical point of view means brittle behaviour of the material and limited applicability in applications requiring toughness.

Conventionally produced steel with subsequent heat treatment (WROUGHT + HT – orange colour) provided more balanced mechanical properties. Although the strength characteristics (YS ~1200 MPa, UTS ~1500 MPa) did not reach the level of HIP material, the highest ductility (~11–12 %) was recorded. This condition thus represents an optimal compromise between strength and ductility and confirms the suitability of conventionally processed H13 steel for industrial applications.

Additively manufactured samples with subsequent heat treatment (AB + HT – yellow colour) achieved the lowest values of all monitored parameters (YS ~1100 MPa, UTS ~1350 MPa, ductility ~5 %). This result clearly demonstrates that the combination of additive manufacturing and heat treatment alone does not provide sufficient material quality in terms of mechanical properties.

A substantial enhancement was evident in samples fabricated by additive manufacturing and subsequently exposed to hot isostatic pressing and heat treatment (HIP REC + HT and HIP BONE + HT – green and blue colour). These variants exhibited a yield strength and tensile strength at the level of conventionally processed material (YS ~1300 MPa, UTS ~1550 MPa) and a ductility of approximately 8–9 %. The results therefore suggest that the combination of HIP and heat treatment can significantly reduce the shortcomings of additively manufactured semi-finished products resulting from microstructural defects (pores, heterogeneities) and bring their mechanical properties closer to those of conventional materials.

In summary, it can be concluded that samples treated with HIP, without undergoing a heat treatment, exhibit the highest levels of strength, yet demonstrate a complete absence of adequate

ductility. The utilisation of additively manufactured material alone does not yield the requisite mechanical parameters; however, the combination of HIP and heat treatment enables the properties to be aligned with those of conventionally processed material. However, conventionally produced H13 steel with heat treatment continues to offer the optimal combination of strength and toughness, which currently renders it the most advantageous option in terms of application.

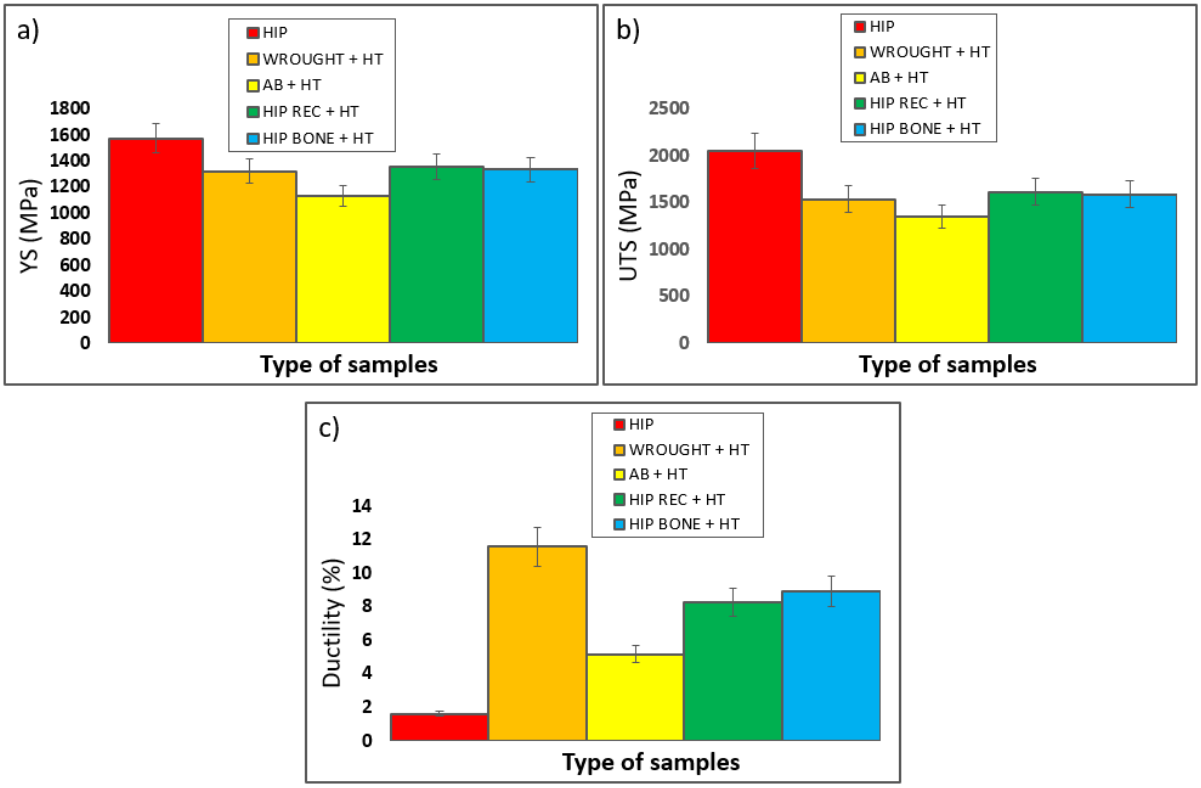

Fig. 19 Mechanical properties of samples a) yield strength, b) ultimate tensile strength, c) ductility

4.4.2 Surface fracture observation

Fig. 20 presents the tensile test, which was conducted under microscopic observation. Row a) corresponds to the AB + HT sample, row b) corresponds to the HIP REC + HT sample, and row c) corresponds to the conventional material. On initial observation, the structures appear to be entirely dissimilar. In the AB sample, individual printed lines are discernible, including the gaps between them (mostly visible in the second image). The third image reveals the presence of pits. During the test, cracks propagate along defects in the microstructure; in this instance, porosity can be identified as a result of insufficient sintering during the process.

The HIP process led to a substantial reduction in porosity. Fine pitting morphology can be observed in the area of damage. Cracks are observed to propagate in the weakest part of the microstructure, which is hypothesised to be the remnants of porosity following HIP. The structure under scrutiny appears to be relatively coarse-grained. The occurrence of larger pits is more prevalent in areas exhibiting increased porosity.

The images in row c) illustrate conventional heat-treated materials. The morphology is distinctly divergent. It is evident that the surface of the material exhibits a high degree of porosity, as well as a significant number of fissures. The presence of inclusions within the material has been identified as a potential causative factor. The small facets are malleable.

The porosity of the samples was measured post-HIP using a CT scan, with a result of 0.48 % being obtained. A comparison of the original value of the AB sample (4.76 %) and the value of the HTAM sample (1.87 %) reveals a significant improvement.

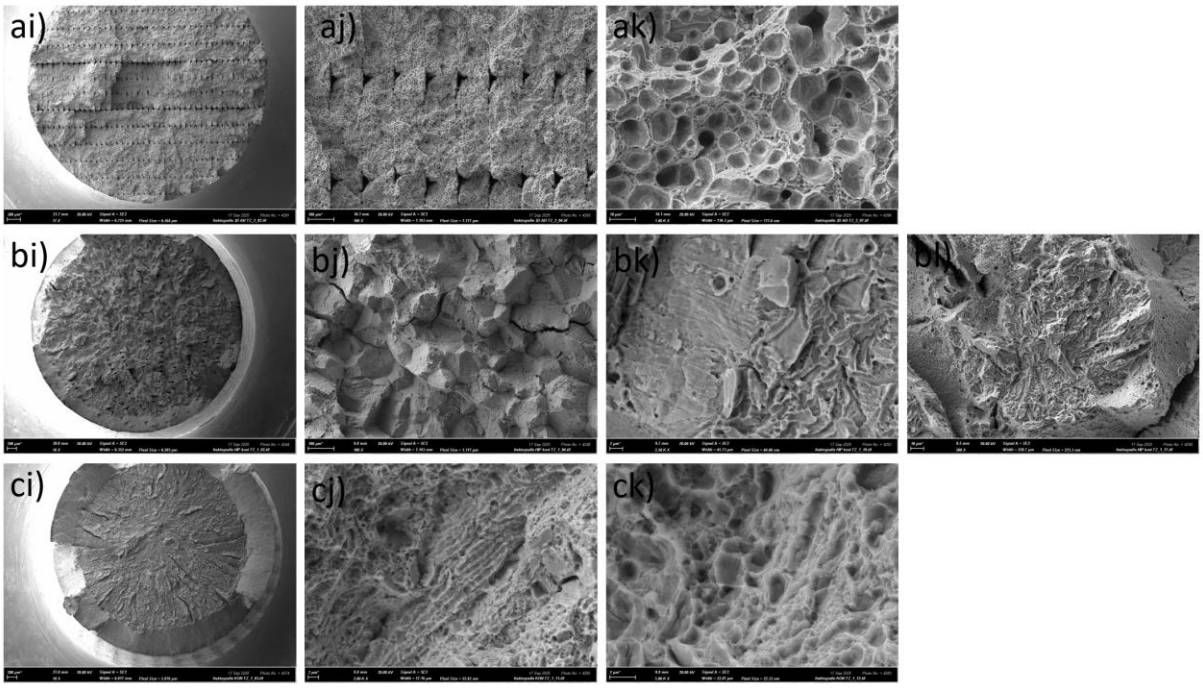

Fig. 20 Images of samples after tensile a) AB + HT samples, b) HIP REC + HT, c) WROUGHT + HT

5 DISCUSSION

The experimental and analytical work presented in this dissertation elucidates the multifaceted relationships among processing parameters, microstructural evolution, and mechanical as well as machining performance of H13 tool steel fabricated using material extrusion (MEX). The present study established quantitative correlations between porosity, densification kinetics, and the mechanical behaviour of additively manufactured H13 through systematic variation of process stages, namely printing, debinding, sintering, heat treatment, and hot isostatic pressing (HIP). The results contribute to a broader understanding of metal extrusion-based additive manufacturing, thereby bridging the gap between low-cost, polymer-based techniques and high-end powder bed fusion (PBF) processes such as selective laser melting (SLM) or electron beam melting (EBM). AM H13 tool steel does not meet the standards required for industrial use after printing. For this reason, the properties of this steel were examined and a study of the machinability of the material was conducted. The key findings are listed below. The input material contains metal particles in a uniform distribution. The composition of the elements is identical to that of H13 tool steel. The printing strategy plays an important role in the resulting mechanical properties. During the creation of the part, individual trajectories are set, and pores may form during printing.

The as-built MEX specimens exhibited an average porosity of approximately 4.76 %, corresponding to an ultimate tensile strength (UTS) of approximately 1200 MPa and ductility of below 1,5 %. These outcomes align with the well-established premise that pore morphology and distribution are critical determinants of load-bearing capacity in additively manufactured steels. The phenomenon of residual pores is attributed to three primary factors:

- incomplete removal of binders,
- non-uniform shrinkage during the sintering process,
- and limited neck formation between metallic particles.

Samples in the as-built state intended for tensile testing printed vertically showed significantly lower UTS compared to samples printed horizontally. In vertically printed samples, it can be seen that there is a separation between the individual layers. Probably, the layers did not fully bond during sintering. For this reason, it would be appropriate to focus on the sintering process. The microstructure of the as-built samples showed a large number of pores in the material. After removing the binder before sintering, voids are created that must be filled to form a non-porous body. The two-phase debinding process reduces debinding time. In the first phase, soluble polymers are dissolved and a porous structure is created, which allows the second part of the binder to escape during the thermal debinding process.

The subsequent application of conventional heat treatment resulted in a significant enhancement of densification and microstructural uniformity, with porosity reduced to approximately 1.87 %. This was accompanied by an enhancement in yield and tensile strength, thus confirming the formation of a martensitic structure.

The most significant enhancement was observed following a combination of HIP and HT. The application of isotropic pressure at elevated temperature by HIP effectively eliminated internal porosity, thereby enabling solid-state diffusion and closure of sub-micron voids. The resulting porosity, reduced to approximately 0.48 %. The mechanical performance of these samples – yield strength ~1300 MPa, UTS ~1550 MPa, and ductility ~8 % – is comparable to that of SLM-processed H13 (Lei et al. [38]) or EBM manufactured tool steel (Kahlert et al. [39]). The outcomes of this study lend further credence to the hypothesis that MEX, when subjected to adequate post-processing, can generate mechanical properties that are well-suited for challenging tooling applications.

A comparison with literature data underscores both the limitations and advantages of extrusion-based additive manufacturing. PBF techniques, such as SLM, have been demonstrated to yield results of high density (typically >99.5 %) and superior surface quality. However, these techniques are encumbered by high equipment costs, limited build volumes, and stringent safety protocols necessitated by powder reactivity. Conversely, MEX provides a cost-effective and environmentally safer alternative that does not necessitate the use of laser optics or a controlled atmosphere during printing. The trade-off is primarily in initial part density and surface finish, which can be compensated for by adequate post-processing.

For comparison, Mertens et al. [62] achieved 1965 MPa tensile strength in SLM H13, whereas the HIP + HT MEX samples approached 1550 MPa. While this variation is substantial for high-stress components, it is deemed acceptable for general tooling applications, particularly when taking into account MEX's reduced cost and accessibility. Nandwana et. al [40] reported that H13 tool steel produced via binder jet additive manufacturing and subsequently processed by hot isostatic pressing (HIP) followed by heat treatment (HT) achieved an ultimate tensile strength of 1836 MPa, surpassing that of conventionally manufactured H13 steel.

Machinability testing of MEX H13 revealed a strong influence of microstructural condition and residual porosity on surface integrity and tool wear. As-built samples exhibited the highest cutting forces and surface roughness, attributable to microvoid collapse and hard-particle abrasion along tool-workpiece interfaces. The augmented feed per tooth served to amplify these effects, thereby accelerating flank wear and degrading surface finish.

Tool wear measurement appears to be predictable. The highest VB values were achieved under the highest cutting conditions, while the lowest VB values were achieved under the lowest cutting conditions. It was found that in the case of machining without the use of machining fluid, the tool wear value is lower compared to machining with the use of process fluid.

Not using process fluid also had a positive effect on the measurement of cutting forces during the process, which showed a more stable course during the process. This is probably due to lower thermal stress on the tool, where there are no sudden changes in temperature as in the case of using cutting fluid. Machining without the use of process fluid not only has a positive effect on the machining process but also reduces the overall financial costs of the process.

Of the cutting conditions examined, feed per tooth has the greatest effect on surface roughness, while cutting speed does not play a significant role. To achieve the best surface quality, the lowest cutting conditions and machining without the use of process fluid are recommended.

The DoAZ size increased with increasing cutting conditions, which affected the surface microhardness and residual stress. The machined surface layer showed higher microhardness values compared to the as-built sample, probably due to smaller grain size, higher KAM parameter, and predominant compressive residual stress. The HTAM sample showed the lowest deformation hardening values and the highest cutting forces, while the AB sample showed the highest hardening values and the lowest cutting forces. It is probably due to the fact that AB sample showed lowest hardness and could be more hardened when machining. The HTW sample showed tensile stress, unlike the pressed samples, in which compressive stress was measured.

The findings of this study are of particular pertinence to the domains of aerospace, automotive, and energy, wherein the utilisation of H13 tool steel is prevalent under conditions of elevated thermal and mechanical stress.

CONCLUSION

The present dissertation study has addressed the challenges and opportunities associated with advanced technologies for 3D printing of metallic components, with particular emphasis on the material extrusion (MEX) process and subsequent machining. The present thesis constitutes a significant contribution to the field, having been derived from comprehensive experimental investigations. These investigations have facilitated a more profound comprehension of the interplay between process parameters, microstructural evolution, and the mechanical and technological properties of H13 tool steel components fabricated through additive manufacturing processes. The outcomes of this study offer both scientific insights and practical guidelines for the broader implementation of these methods in industrial contexts.

The initial phase of the research indicated that as-built samples produced by MEX exhibited elevated porosity and diminished mechanical performance in comparison to conventionally manufactured materials. Porosity levels of **4.76 %** were measured in as-printed samples, with the result that these levels had a direct influence on tensile strength, ductility, and residual stresses. The mechanical properties of these as-built parts reflected the limitations of the extrusion-debinding-sintering process chain. Tensile testing was conducted, yielding ultimate tensile strength (UTS) values ranging from **950 to 1100 MPa**, with yield strength (YS) not exceeding **900 MPa**. Ductility remained low, typically below **1.5 %,** with fracture surfaces showing brittle features related to inter-layer defects. These findings indicate that while MEX offers cost and accessibility advantages, its direct use for highly loaded tooling applications is restricted without appropriate post-processing. In relation to the surface roughness of the as-built sample, it has been established that machining is a prerequisite, given that the measured Ra roughness value was **6.45 µm** and the Rz value was **24.3 µm**.

Subsequent heat treatment enhanced hardness and microstructural homogeneity; however, porosity continued to be a limiting factor. The machining experiments conducted on heat-treated MEX samples yielded valuable insights into tool wear, cutting forces, and surface integrity. In comparison with conventionally produced steel, MEX-manufactured samples demonstrated higher cutting forces and accelerated flank wear of carbide tools. This accelerated wear can be attributed to the presence of internal porosity, which functioned as stress concentrators and abrasive sites. Nevertheless, it was demonstrated that acceptable surface roughness (Ra ≈ 0.8–1.2 µm) could be achieved under optimised cutting conditions, thereby indicating that functional surface quality can be assured through the implementation of meticulous machining strategies.

In view of the data obtained, it is clear that further studies are required in order to obtain a larger number of relevant results and formulate conclusions. The following conclusions can be drawn from the available sources. Porosity has been demonstrated to have a significant impact on the measured parameters, including cutting forces, tool wear and surface roughness. A number of methodologies were advanced during the course of the work with a view to reducing porosity. The most effective method of material compression appears to be the **HIP** process, in which the material is compressed at elevated temperatures and the pores are closed. The initial measured porosity of the AB sample was 4.76 %, which was reduced to **0.48 %** through the use of HIPing. In accordance with the anticipated outcomes, a decline in porosity was observed, accompanied by an enhancement in the mechanical properties of the material. The material's ultimate tensile strength (UTS) was recorded at **1550 MPa**, its yield strength (YS) at **1300 MPa**, and its ductility was determined to be **8 %**.

Future research should focus on optimising feedstock composition, sintering, and binder removal to reduce porosity and improve green body integrity. Further studies on the fatigue, thermal, and wear performance of HIP-processed MEX steels, as well as on sustainable filament recyclability, are also recommended.

In conclusion, this work has shown that material extrusion can be developed into a competitive additive manufacturing method for tool steels when supported by appropriate post-processing and machining. The combination of experimental data, mechanical testing, and machinability analysis presented here contributes to both the academic understanding and industrial utilization of this emerging technology. By bridging the gap between low-cost extrusion printing and high-performance tooling applications, the thesis provides a foundation for further innovation and practical adoption of additive manufacturing in the tool and die industry.

REFERENCES

[1] *F42 Committee, Terminology for Additive Manufacturing Technologies, ASTM International, West Conshohocken, PA, 2012, https://doi.org/10.1520/F2792- 12*.

[2] INTERNATIONAL ORGANIZATION FOR STANDARDIZATION. *ISO/ASTM 52900:2021 Additive manufacturing — General principles — Fundamentals and vocabulary*. 2021.

[3] DÖRFERT, R.; ZHANG, J.; CLAUSEN, B.; FREISSE, H.; SCHUMACHER, J. et al. Comparison of the fatigue strength between additively and conventionally fabricated tool steel 1.2344. Online. *Additive Manufacturing*. 2019, roč. 27, s. 217-223. ISSN 22148604. Dostupné z: https://doi.org/10.1016/j.addma.2019.01.010. [cit. 2024-04-19].

[4] ARMILLOTTA, Antonio; BARAGGI, Raffaello a FASOLI, Simone. SLM tooling for die casting with conformal cooling channels. Online. *The International Journal of Advanced Manufacturing Technology*. 2014, roč. 71, č. 1-4, s. 573-583. ISSN 0268-3768. Dostupné z: https://doi.org/10.1007/s00170-013-5523-7. [cit. 2024-04-19].

[5] NING, Angang; MAO, Wenwen; CHEN, Xichun; GUO, Hanjie a GUO, Jing. Precipitation Behavior of Carbides in H13 Hot Work Die Steel and Its Strengthening during Tempering. Online. *Metals*. 2017, roč. 7, č. 3. ISSN 2075-4701. Dostupné z: https://doi.org/10.3390/met7030070. [cit. 2024-04-19].

[6] SHAYFULL, Z.; SHARIF, S.; ZAIN, Azlan Mohd.; GHAZALI, M. F. a SAAD, R. Mohd. Potential of Conformal Cooling Channels in Rapid Heat Cycle Molding: A Review. Online. *Advances in Polymer Technology*. 2014, roč. 33, č. 1. ISSN 0730-6679. Dostupné z: https://doi.org/10.1002/adv.21381. [cit. 2024-04-19].

[7] CHOI, J. a CHANG, Y. Characteristics of laser aided direct metal/material deposition process for tool steel. Online. *International Journal of Machine Tools and Manufacture*. 2005, roč. 45, č. 4-5, s. 597-607. ISSN 08906955. Dostupné z: https://doi.org/10.1016/j.ijmachtools.2004.08.014. [cit. 2024-04-19].

[8] PARK, Jun Seok; PARK, Joo Hyun; LEE, Min-Gyu; SUNG, Ji Hyun; CHA, Kyoung Je et al. Effect of Energy Input on the Characteristic of AISI H13 and D2 Tool Steels Deposited by a Directed Energy Deposition Process. Online. *Metallurgical and Materials Transactions A*. 2016, roč. 47, č. 5, s. 2529-2535. ISSN 1073-5623. Dostupné z: https://doi.org/10.1007/s11661-016-3427-5. [cit. 2024-04-19].

[9] PINKERTON, Andrew J. a LI, Lin. Direct additive laser manufacturing using gas- and water-atomised H13 tool steel powders. Online. *The International Journal of Advanced Manufacturing Technology*. 2005, roč. 25, č. 5-6, s. 471-479. ISSN 0268-3768. Dostupné z: https://doi.org/10.1007/s00170-003-1844-2. [cit. 2024-04-19].

[10] MERTENS, R.; VRANCKEN, B.; HOLMSTOCK, N.; KINDS, Y.; KRUTH, J.-P. et al. Influence of Powder Bed Preheating on Microstructure and Mechanical Properties of H13 Tool Steel SLM Parts. Online. *Physics Procedia*. 2016, roč. 83, s. 882-890. ISSN 18753892. Dostupné z: https://doi.org/10.1016/j.phpro.2016.08.092. [cit. 2024-04-19].

[11] HOLZWEISSIG, Martin Joachim; TAUBE, Alexander; BRENNE, Florian; SCHAPER, Mirko a NIENDORF, Thomas. Microstructural Characterization and Mechanical Performance of Hot Work Tool Steel Processed by Selective Laser Melting. Online. *Metallurgical and Materials Transactions B*. 2015, roč. 46, č. 2, s. 545-549. ISSN 1073-5615. Dostupné z: https://doi.org/10.1007/s11663-014-0267-9. [cit. 2024-04-19].

[12] ČSN EN ISO 6892-1, *Metallic materials - Tensile testing - Part 1: Method of test at room temperature*. 2021.

[13] NOVÁK, Martin; HAUSNEROVA, Berenika; PATA, Vladimir a SANETRNIK, Daniel. On the possibilities of merging additive manufacturing and powder injection molding in the production of metal parts. Online. *Rapid Prototyping Journal*. 2024, roč. 30, č. 11, s. 50-58. ISSN 1355-2546. Dostupné z: https://doi.org/10.1108/RPJ-02-2023-0047. [cit. 2024-04-08].

[14] ÅSBERG, M.; FREDRIKSSON, G.; HATAMI, S.; FREDRIKSSON, W. a KRAKHMALEV, P. Influence of post treatment on microstructure, porosity and mechanical properties of additive manufactured H13 tool steel. Online. *Materials Science and Engineering: A*. 2019, roč. 742, s. 584-589. ISSN 09215093. Dostupné z: https://doi.org/10.1016/j.msea.2018.08.046. [cit. 2025-07-01].

[15] FRYZOWICZ, K.; DZIURKA, R.; BARDO, R.; MARCISZKO-WIĄCKOWSKA, M. a BAŁA, P. Point-by-point laser exposure for crack susceptibility reduction in Powder Bed Fusion processing of H11 tool steel. Online. *Journal of Materials Processing Technology*. 2023, roč. 316. ISSN 09240136. Dostupné z: https://doi.org/10.1016/j.jmatprotec.2023.117946. [cit. 2024-04-08].

[16] CHE-HARON, C.H. a JAWAID, A. The effect of machining on surface integrity of titanium alloy Ti–6% Al–4% V. Online. *Journal of Materials Processing Technology*. 2005, roč. 166, č. 2, s. 188-192. ISSN 09240136. Dostupné z: https://doi.org/10.1016/j.jmatprotec.2004.08.012. [cit. 2025-07-04].

[17] BAI, Yuchao; ZHAO, Cuiling; YANG, Jin; HONG, Ruochen; WENG, Can et al. Microstructure and machinability of selective laser melted high-strength maraging steel with heat treatment. Online. *Journal of Materials Processing Technology*. 2021, roč. 288. ISSN 09240136. Dostupné z: https://doi.org/10.1016/j.jmatprotec.2020.116906. [cit. 2024-04-24].

[18] EL-HOSSAINY, T. M.; EL-ZOGHBY, A. A.; BADR, M. A.; MAALAWI, K. Y. a NASR, M. F. Cutting Parameter Optimization when Machining Different Materials. Online. *Materials and Manufacturing Processes*. 2010, roč. 25, č. 10, s. 1101-1114. ISSN 1042-6914. Dostupné z: https://doi.org/10.1080/10426914.2010.480998. [cit. 2024-04-24].

[19] JEYAKUMAR, S.; MARIMUTHU, K. a RAMACHANDRAN, T. Prediction of cutting force, tool wear and surface roughness of Al6061/SiC composite for end milling operations using RSM. Online. *Journal of Mechanical Science and Technology*. 2013, roč. 27, č. 9, s. 2813-2822. ISSN 1738-494X. Dostupné z: https://doi.org/10.1007/s12206-013-0729-z. [cit. 2024-04-24].

[20] VAZIRI, M. R.; NOWRUZPOUR MEHRIAN, S. M.; NAEI, M. H. a SHEIKH AHMAD, Jamal Y. Modification of Shock Resistance for Cutting Tools Using Functionally Graded Concept in Multilayer Coating. Online. *Journal of Thermal Science and Engineering Applications*. 2015, roč. 7, č. 1. ISSN 1948-5085. Dostupné z: https://doi.org/10.1115/1.4028982. [cit. 2024-04-24].

[21] PELIKÁN, Lukáš; SLANÝ, Michal; STRÁNSKÝ, Ondřej; BERÁNEK, Libor; PITRMUC, Zdeňek et al. Novel drill geometries for dry drilling of stainless steel. Online. *Journal of Manufacturing Processes*. 2023, roč. 92, s. 500-520. ISSN 15266125. Dostupné z: https://doi.org/10.1016/j.jmapro.2023.03.006. [cit. 2024-04-24].

[22] YAMAGUCHI, Kenji; FUJITA, Tsuyoshi; KONDO, Yasuo; SAKAMOTO, Satoshi; YAMAGUCHI, Mitsugu et al. Effects of Cooling Conditions on Thermal Crack Initiation of Brittle Cutting Tools during Intermittent Cutting. Online. *Key Engineering Materials*. 2015, roč. 656-657, s. 237-242. ISSN 1662-9795. Dostupné z: https://doi.org/10.4028/www.scientific.net/KEM.656-657.237. [cit. 2024-04-24].

[23] OLIVEIRA, A. R.; JARDINI, A. L. a DEL CONTE, E. G. Effects of cutting parameters on roughness and residual stress of maraging steel specimens produced by additive manufacturing. Online. *The International Journal of Advanced Manufacturing Technology*. 2020, roč. 111, č. 9-10, s. 2449-2459. ISSN 0268-3768. Dostupné z: https://doi.org/10.1007/s00170-020-06309-3. [cit. 2024-04-25].

[24] LIAO, Zhirong; LA MONACA, Andrea; MURRAY, James; SPEIDEL, Alistair; USHMAEV, Dmitrii et al. Surface integrity in metal machining - Part I: Fundamentals of surface characteristics and formation mechanisms. Online. *International Journal of Machine Tools and Manufacture*. 2021, roč. 162. ISSN 08906955. Dostupné z: https://doi.org/10.1016/j.ijmachtools.2020.103687. [cit. 2024-04-25].

[25] ASLANTAS, K. a ALATRUSHI, L. K. H. Experimental Study on the Effect of Cutting Tool Geometry in Micro-Milling of Inconel 718. Online. *Arabian Journal for Science and Engineering*. 2021, roč. 46, č. 3, s. 2327-2342. ISSN 2193-567X. Dostupné z: https://doi.org/10.1007/s13369-020-05034-z. [cit. 2024-04-25].

[26] ZAIDI, Sajid Raza; UL QADIR, Najam; JAFFERY, Syed Husain Imran; KHAN, Muhammad Ali; KHAN, Mushtaq et al. Statistical Analysis of Machining Parameters on Burr Formation, Surface Roughness and Energy Consumption during Milling of Aluminium Alloy Al 6061-T6. Online. *Materials*. 2022, roč. 15, č. 22. ISSN 1996-1944. Dostupné z: https://doi.org/10.3390/ma15228065. [cit. 2024-04-25].

[27] PHAM, Thi-Hoa; NGUYEN, Duc-Toan; BANH, Tien-Long a TONG, Van-Canh. Experimental study on the chip morphology, tool–chip contact length, workpiece vibration, and surface roughness during high-speed face milling of A6061 aluminum alloy. Online. *The Journal of Engineering Manufacture*. 2019, roč. 234, č. 3. Dostupné z: https://doi.org/10.1177/0954405419863. [cit. 2024-04-25].

[28] ZHANG, Xuewei; YU, Tianbiao; DAI, Yuanxing; QU, Sheng a ZHAO, Ji. Energy consumption considering tool wear and optimization of cutting parameters in micro milling process. Online. *International Journal of Mechanical Sciences*. 2020, roč. 178. ISSN 00207403. Dostupné z: https://doi.org/10.1016/j.ijmecsci.2020.105628. [cit. 2024-04-25].

[29] ALVES, U. C.; HASSUI, A.; DE OLIVEIRA, M. F.; NETO, P. I. a VENTURA, C. E. H. Microstructural and machinability aspects of electron beam melted Ti–6Al–4V with different building orientations. Online. *Progress in Additive Manufacturing*. 2023, roč. 8, č. 2, s. 131-141. ISSN 2363-9512. Dostupné z: https://doi.org/10.1007/s40964-022-00317-3. [cit. 2024-04-24].

[30] NANDWANA, Peeyush; KANNAN, Rangasayee a SIDDEL, Derek. Microstructure evolution during binder jet additive manufacturing of H13 tool steel. Online. *Additive Manufacturing*. 2020, roč. 36. ISSN 22148604. Dostupné z: https://doi.org/10.1016/j.addma.2020.101534. [cit. 2025-07-01].

[31] LI, Shuhan; DENG, Hanwen; LAN, Xinqiang; HE, Bing; LI, Xiangyou et al. Developing cost-effective indirect manufacturing of H13 steel from extrusion-printing to post-processing. Online. *Additive Manufacturing*. 2023, roč. 62. ISSN 22148604. Dostupné z: https://doi.org/10.1016/j.addma.2022.103384. [cit. 2024-04-25].

[32] FONSECA, Eduardo B.; GABRIEL, André H.G.; ÁVILA, Julián A.; VAZ, Rodolpho F.; VALIM, Diego B. et al. Fracture toughness and wear resistance of heat-treated H13 tool steel processed by laser powder bed fusion. Online. *Additive Manufacturing*. 2023, roč. 78. ISSN 22148604. Dostupné z: https://doi.org/10.1016/j.addma.2023.103862. [cit. 2025-07-01].

[33] SAN-JUAN, M.; MARTÍN, Ó.; TIEDRA, M. del P. de; SANTOS, F.J.; LÓPEZ, R. et al. Study of Cutting Forces and Temperatures in Milling of AISI 316L. Online. *Procedia*

Engineering. 2015, roč. 132, s. 500-506. ISSN 18777058. Dostupné z: https://doi.org/10.1016/j.proeng.2015.12.525. [cit. 2025-07-02].

[34] ZHA, Jun; YUAN, Zelong; ZHANG, Hangcheng; LI, Yipeng a CHEN, Yaolong. Nickel-Based Alloy Dry Milling Process Induced Material Softening Effect. Online. *Materials*. 2020, roč. 13, č. 17. ISSN 1996-1944. Dostupné z: https://doi.org/10.3390/ma13173758. [cit. 2025-07-02].

[35] ABHANG, L.B. a HAMEEDULLAH, M. Chip-Tool Interface Temperature Prediction Model for Turning Process. Online. *International Journal of Engineering Science and Technology*. 2010, vol. 2, no. 4, s. 382-393. ISSN 0975-5462. Dostupné z: https://scholar.google.com/scholar_lookup?title=Chip-Tool%20Interface%20Temperature%20Prediction%20Model%20for%20Turning%20Process%2C%20International%20Journal%20Of%20Engineering%20Science%20And&author=L.B.%20Abhang&publication_year=2010&pages=382-393. [cit. 2025-07-02].

[36] DENKENA, Berend; ABELE, Eberhard; BRECHER, Christian; DITTRICH, Marc-André; KARA, Sami et al. Energy efficient machine tools. Online. *CIRP Annals*. 2020, roč. 69, č. 2, s. 646-667. ISSN 00078506. Dostupné z: https://doi.org/10.1016/j.cirp.2020.05.008. [cit. 2025-07-02].

[37] DESHPANDE, Soham a DESHPANDE, Yogesh. A Review On Cooling Systems Used In Machining Processes. Online. *Materials Today: Proceedings*. 2019, roč. 18, s. 5019-5031. ISSN 22147853. Dostupné z: https://doi.org/10.1016/j.matpr.2019.07.496. [cit. 2025-07-02].

[38] LEI, Fei; WEN, Tao; YANG, Feipeng; WANG, Jianying; FU, Junwei et al. Microstructures and Mechanical Properties of H13 Tool Steel Fabricated by Selective Laser Melting. Online. *Materials*. 2022, vol. 15, no. 7, s. 2686. ISSN 1996-1944. Dostupné z: https://doi.org/10.3390/ma15072686. [cit. 2025-07-29].

[39] KAHLERT, Moritz; BRENNE, Florian; VOLLMER, Malte a NIENDORF, Thomas. Influence of Microstructure and Defects on Mechanical Properties of AISI H13 Manufactured by Electron Beam Powder Bed Fusion. Online. *Journal of Materials Engineering and Performance*. 2021, roč. 30, č. 9, s. 6895-6904. ISSN 1059-9495. Dostupné z: https://doi.org/10.1007/s11665-021-06059-7. [cit. 2024-05-14].

[40] NANDWANA, Peeyush; KANNAN, Rangasayee; UNOCIC, Kinga A.; FANCHER, Christopher M.; GOLDSBY, Desarae et al. High temperature tensile properties of H13 tool steel fabricated via binder jet additive manufacturing. Online. *Journal of Materials Research and Technology*. 2025, vol. 37, s. 2577-2585. ISSN 2238-7854. Dostupné z: https://doi.org/10.1016/j.jmrt.2025.06.168. [cit. 2025-09-24].